ADVANCING EARTH AND SPACE SCIENCE

JGR Solid Earth

RESEARCH ARTICLE
10.1029/2022JB025858

Key Points:

- Grain-growth chemical remanent magnetization (gCRM) acquisition is modeled for interacting single-domain particles using Preisach theory
- gCRM intensities are less sensitive to changes in interactions and more sensitive to coercivity changes than thermal remanent magnetizations
- Arai plots for gCRM are concave-up with the degree of curvature increasing with higher interactions and lower coercivities

Correspondence to:
E. B. Baker,
evelyn.baker15@imperial.ac.uk

Citation:
Baker, E. B., & Muxworthy, A. R. (2023). Using Preisach theory to evaluate chemical remanent magnetization and its behavior during Thellier-Thellier-Coe paleointensity experiments. *Journal of Geophysical Research: Solid Earth*, *128*, e2022JB025858. https://doi.org/10.1029/2022JB025858

Received 18 OCT 2022
Accepted 2 FEB 2023

Author Contributions:
Conceptualization: Adrian R. Muxworthy
Formal analysis: Evelyn B. Baker
Funding acquisition: Adrian R. Muxworthy
Investigation: Evelyn B. Baker, Adrian R. Muxworthy
Methodology: Evelyn B. Baker, Adrian R. Muxworthy
Project Administration: Adrian R. Muxworthy
Resources: Adrian R. Muxworthy
Software: Evelyn B. Baker, Adrian R. Muxworthy
Supervision: Adrian R. Muxworthy
Writing – original draft: Evelyn B. Baker
Writing – review & editing: Evelyn B. Baker, Adrian R. Muxworthy

Using Preisach Theory to Evaluate Chemical Remanent Magnetization and Its Behavior During Thellier-Thellier-Coe Paleointensity Experiments

Evelyn B. Baker[1] and **Adrian R. Muxworthy**[1,2]

[1]Department of Earth Science and Engineering, Imperial College London, London, UK, [2]Department of Earth Sciences, University College London, London, UK

Abstract The behavior of grain-growth chemical remanent magnetizations (gCRM) are investigated for different coercivity and magnetostatic-interaction-field distributions and acquisition conditions using a thermally activated Preisach model for assemblages of interacting single-domain grains. A new growth-rate dependent equation was derived, from which it was found that gCRM intensity is over 10% more sensitive to growth rate than previously modeled. We compare the gCRM results to the behavior of thermoremanences (TRM). gCRMs are two times more sensitive to changes in coercivity distribution, whereas TRMs are four times more sensitive to changes in magnetostatic interactions. The Thellier-Thellier-Coe paleointensity protocol was simulated in Preisach space, and gCRMs were found to produce concave-up Arai plots with pTRM checks which plot to the left of the Arai plot and positive partial-TRM tail checks that increase with magnetostatic interactions. This often leads to the failure of selection criteria, but high-temperature segments can pass the criteria for weakly interacting gCRMs; these estimates can underestimate the field by up to 66%.

Plain Language Summary Rocks containing magnetic minerals usually magnetically record the Earth's magnetic field during their formation acquiring a remanent magnetization. It is known that many rocks record a thermoremanent magnetization during cooling from high temperatures, however, it is also common for magnetic minerals to acquire magnetic remanence during the growth of magnetic minerals at ambient temperatures (grain-growth chemical remanent magnetization, gCRM). It is important to have an understanding of the magnetic remanence recording mechanism if we are to understand ancient magnetic recordings which can hold information about the formation of our Solar System and the habitability of the Earth. Most previous theoretical and experimental studies have focused on thermoremanence acquisition, and have ignored gCRM acquisition theory. We have undertaken a theoretical investigation of gCRM acquisition, and find gCRMs respond very differently to thermoremanences during simulated standard laboratory measurements. In particular, we find that gCRMs cannot be used to determine ancient magnetic field intensities using conventional methods based on thermoremanence acquisition, as they typically yield underestimates of up to 66%.

1. Introduction

Magnetic minerals within rocks, meteorites and sediments can record the ambient magnetic field during their formation, acquiring remanent magnetizations. There are several recording mechanisms depending on the rock type and mineral formation. For example, a thermoremanent magnetization (TRM) is acquired during cooling from above the constituent minerals' Curie temperatures, and chemical remanent magnetizations (CRM) are acquired if a mineral forms or alters below its Curie temperature. The recording mechanisms of these various remamances differs. Whilst much attention has historically been given to TRM acquisition (e.g., Nagy et al., 2022; Néel, 1949), CRM acquisition is less understood (e.g., Haigh, 1958; Shcherbakov et al., 1996).

CRMs are ubiquitous in nature, for example, magnetic minerals formed via authigenic precipitation in sedimentary systems can acquire CRMs (Elmore et al., 2012), as can igneous rocks subject to high (Yamamoto, 2006) or low temperature oxidation (Bleil & Petersen, 1983). CRMs are known to significantly contribute to paleomagnetic signals, often dominating the remanence (Haigh, 1958; Larson et al., 1982). CRMs have also been frequently shown to be reliable recorders of paleo-directional information, however, determining ancient field intensity (paleointensity) estimates from CRMs has not be achievable, nor is their contribution to TRM-based paleointensity methods, for example, modified Thellier-type methods (Coe, 1967; Thellier & Thellier, 1959), accurately understood nor quantified (Draeger et al., 2006; Gribov et al., 2017; Shcherbakov et al., 2017, 2021).

CRM acquisition processes have been studied both experimentally (e.g., Gribov et al., 2017; Haigh, 1958; Mcclelland & Goss, 1993; Pick & Tauxe, 1991; Stokking & Tauxe, 1987) and theoretically (e.g., Fabian, 2009; Haigh, 1958; McClelland, 1996; Shcherbakov & Sycheva, 2019; Shcherbakov et al., 1996, 2021). Most models have focused on grain-growth CRM (gCRM): a gCRM is acquired when magnetic minerals nucleate and grow in the presence of a field. Other types of CRM are harder to model, for example, CRMs acquired during alteration of magnetic phases (Heider & Dunlop, 1987), are complicated by interactions between the old and new magnetic phases (Almeida et al., 2014; Ge et al., 2014).

Experiments focused on simple gCRMs have proven hard to study due to the difficulty in producing synthetic samples. Despite this, room-temperature gCRMs have been found to reliably record ambient magnetic fields and gCRM intensity is directly proportional to the applied field intensity for weak magnetic fields (e.g., Jiang et al., 2015; Pick & Tauxe, 1991; Stokking & Tauxe, 1990). Although, experimental attempts to quantify the contribution of gCRM to Arai plots used to interpret Thellier-type paleointensity data leave a lot of questions unanswered, for example, synthetic hematite samples carrying gCRMs display variable Arai plot shapes, which is attributed to hematite alteration during heating (Stokking & Tauxe, 1990).

The first theoretical framework for gCRM acquisition was by Haigh (1958) who suggested that gCRM acquistion is a thermally activated process which can be modeled using Néel (1949) theory for non-interacting, magnetically uniform (single domain, SD) grains, whose thermal relaxation time τ is given by:

$$\tau = \tau_0 \exp\left(\frac{\mu_0 H_c M_s v}{2k_B T}\right) \tag{1}$$

where τ_0^{-1} is the atomic attempt frequency, μ_0 is the permeability of free space, v is the grain volume, M_s is the saturation magnetization, H_c is the coercive force, k_B is the Boltzmann constant and T is the temperature. At small volumes magnetic grains are superparamagnetic (SP), that is, they are thermally activated and do not retain a magnetic remanence on the time scale of interest, for example, 60 s for a laboratory measurement. When a particle grows through its blocking volume (v_b), the energy barriers to magnetic moment rotation increase and the grain's magnetic moment becomes stable, that is, it is "blocked" and acquires a remanence.

McClelland (1996) used Néel (1949) theory to model gCRM acquisition and predicted that gCRMs have a lower thermal stability than TRMs. This result was confirmed by Shcherbakov et al. (1996) using a Monte Carlo model for interacting SD assemblages. In subsequent studies, Shcherbakov and co-workers (Shcherbakov & Sycheva, 2019; Shcherbakov et al., 2017, 2021) simulated Thellier-type paleointensity methods and showed that high-temperature gCRMs and thermochemical remanent magnetization (TCRMs), produce concave-up Arai plots; TCRMs were simulated by modeling elevated-temperature grain-growth followed by cooling.

There are inconsistencies between the experimental results and theoretical predictions. For example, experimental studies of CRMs (e.g., Pucher, 1969; Stokking & Tauxe, 1990) found lower CRM/TRM ratios than theoretical studies predict (McClelland, 1996; Shcherbakov et al., 2017), and Arai plots for experimental CRMs display a range of shapes, including the predicted "concave-up" trend (Gendler et al., 2005), but also linear (Stokking & Tauxe, 1990).

In this theoretical study we present a new framework for gCRM acquisition based on a thermally activated Preisach model for interacting SD particles (Preisach, 1935; Roshko & Viddal, 2004; Stancu & Spinu, 1998). Preisach theory is a pictorial representation of magnetic systems, where the location of a particle on the Preisach diagram determines its coercivity and interaction field (Bertotti, 1998; Néel, 1958). We derive an equation to incorporate the growth rate into the gCRM acquisition. We examine gCRMs for a range of magnetic assemblages of magnetite formed under different conditions, and make comparisons to TRMs using the Preisach TRM acquisition model of Muxworthy and Heslop (2011). We also use our model to simulate the behavior of gCRM during Thellier-type paleointensity determinations, and evaluate how gCRMs contributes to Arai plots.

2. Method

To model gCRM acquisition we adapted the TRM Preisach model developed by Muxworthy and Heslop (2011), which uses a thermally activated Preisach model for magnetic assemblages composed of interacting SD grains. In the model we assume that the SD particles are controlled by their shape anisotropy and can be described by Stoner and Wohlfarth (1948) (SW) theory. Each particle is represented as a hysteron defined by the switching fields H_α and H_β. The distribution of hysterons is termed a Preisach distribution $p(h_c, h_s)$ and is rotated 45° with

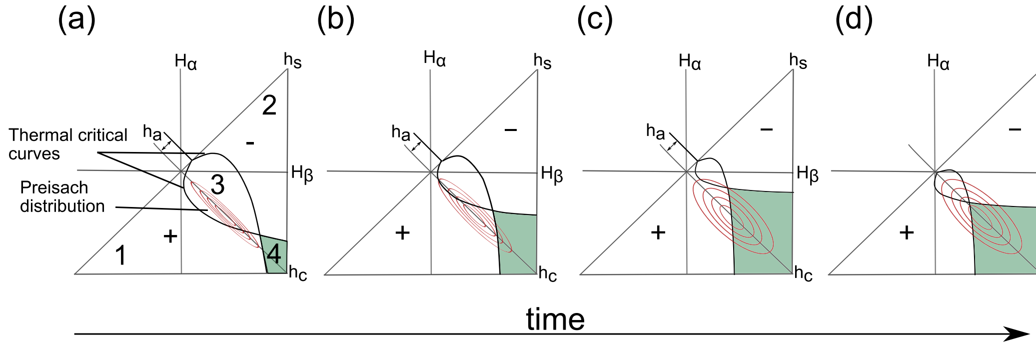

Figure 1. Schematic of thermally activated Preisach diagrams with increasing time during grain-growth chemical remanent magnetization acquisition in the presence of applied field h_a between (a) and (d). In (a) the highlighted zones are: (1) the positive field-blocked zone, (2) the negative field-blocked zone, (3) the superparamagnetic zone and (4) the remanence zone (green). Over time as the volume increases, the Preisach distribution expands and the thermal critical curves contract and the assemblage acquires a remanent magnetization as the Preisach distribution crosses the curves into the remanence zone. The thermal critical curves shift onto the h_c axis when the field is removed, that is, from (c) to (d).

respect to the switching-field space (Figure 1) h_c is the coercivity and h_s is the interaction field in Preisach space. Preisach space for a thermally activated system of particles is split into four regions separated by the thermal critical barriers (Figure 1a): (1) the positive field-blocked region, (2) the negative field-blocked region, (3) the superparamagnetic region and (4) the remanence region (Stancu & Spinu, 1998). The location of the hysteron determines if it carries a magnetic remanence or not. The positions of the thermal critical curves depend upon a particle's properties, temperature and the applied field, and are unique for each particle. The critical barriers rely on a fictional thermal fluctuation field H_f, which is an approximation for the effect of thermal fluctuations in terms of a field. For aligned particles, H_f was defined by Wohlfarth (1984) as

$$H_f = \frac{k_B T}{\mu_0 M_s v_{act}} \tag{2}$$

where v_{act} is the activation volume of the SW particle. v_{act} is related to the actual volume by $v_{act} = v[1 - H/H_k]$ for an SW particle during blocking, where H_k is the anisotropy field, and H is the field the particle experiences (Gaunt, 1986; Lyberatos et al., 1994). For randomly orientated SW particles the thermal critical curves cannot be found analytically, but Pfeiffer (1990) numerically found a simple analytical approximation, which is commonly used (e.g., Muxworthy & Heslop, 2011; Stancu & Spinu, 1998).

2.1. Theoretical Framework for Modeling gCRM Acquisition

To simulate gCRM acquisition, we model how the thermal critical barriers and particle positions evolve with time as the particles grow to their terminal volume. We start with a nucleation diameter for magnetite of 2 nm (Baumgartner et al., 2013). For particles greater than a few nanometers, M_s is independent of v (Penny et al., 2019). This is much below the blocking volume of the minerals of interest, therefore we assume M_s to be independent of v.

As the volumes increase the thermal critical curves contract (Figure 1), and the Preisach distribution expands in the h_s direction up to the width of the input Preisach distribution ($p(h_c, h_s)_0$), to accommodate the increase in magnetostatic interactions experienced by particles as they grow and block. We assume a linear increase (Muxworthy & Dunlop, 2002; Muxworthy & Williams, 2005).

Initially the particles are in the SP region (Figure 1a). As the particles grow in an applied field, they cross into the remanence region acquiring a remanent magnetization (Figures 1a–1c). The probability of an individual SW particle being aligned with the field during blocking is given by (Néel, 1949)

$$M_{eq} = v M_s \tanh\left(\frac{\mu_0 M_s v_b H}{k_B T}\right) \tag{3}$$

where H is the net magnetic field, that is, H_a–$H_s(v_b)$, and H_a is the applied field and $H_s(v_b)$ is the interaction field at blocking in switching field space (H_α, H_β) (Muxworthy & Heslop, 2011; Stancu & Spinu, 1998). After the

10.1029/2022JB025858

particles have stopped growing, to determine the gCRM the external field is set to zero, centering the thermal critical curves about $h_s = 0$ (Figure 1d).

In the gCRM acquisition model the locations of the Preisach distribution and thermal critical barriers are found at discrete time steps, whereas in nature grain growth is a continuous process. Therefore, to accommodate the growth rate of the particles, we include an effective time t^C_{eff} dependent on growth rate; this is similar in approach to the effective cooling and/or heating time used elsewhere (Borcia et al., 2002; Muxworthy & Heslop, 2011). Here we derive t^C_{eff} following the methods of Dodson and McClelland-Brown (1980) and Berndt and Muxworthy (2017) who collectively examined both heating and cooling rates. To achieve this we solve a standard form of the master equation for SW particles incorporating the Néel (1949) relaxation time equation, given by

$$\frac{dn}{dt} = (n_{eq} - n)\frac{1}{\tau_0}\exp\left(\frac{-\varepsilon}{k_B T}\right) \tag{4}$$

where n is the total number of SW particles, n_{eq} is the equilibrium state and ε is the energy of a particle at a specific volume and temperature as a function of time t. We use the assumption from Dodson and McClelland-Brown (1980) that the energy balance term is zero at $t = 0$ as the particles are initially all SP, and over the blocking region the exponent and n_{eq} vary linearly with time. We also assume that the diameter growth rate is linear with time, which is a common first-order approximation for crystal growth in the laboratory and in nature (Baumgartner et al., 2013; Eberl et al., 2002). With these assumptions and using the formulations of Dodson and McClelland-Brown (1980), we write

$$\frac{\varepsilon}{k_B T} = \frac{t}{\theta} \tag{5}$$

where θ is the rate constant, the time taken for τ to increase by a factor e, Euler's constant (Dodson & McClelland-Brown, 1980). A lengthy derivation in the appendix of Dodson and McClelland-Brown (1980) (not repeated here) gives an expression for the energy term at the blocking condition, that is,

$$\frac{\varepsilon}{k_B T} = \ln\left(\frac{\gamma\theta}{\tau_0}\right) \tag{6}$$

where γ is the exponential of Euler's constant. Berndt and Muxworthy (2017) showed that the effective time for cooling, t^T_{eff}, is equivalent to $\gamma\theta_T$ over the blocking region, where θ_T is the cooling rate constant. To derive t^C_{eff}, we first note that ε is dependent only on $v(t)$, and as anisotropy is controlled by shape anisotropy, $\varepsilon(v(t)) = \mu_0 v(t) H_k Ms/2$. Next we differentiate Equation 5 with respect to time. We then apply the chain rule and express $\varepsilon(v(t))$ in terms of v, yielding $d\varepsilon(v(t))/dv = \varepsilon(v(t))/v$. Introducing the constant γ, Equation 5 now becomes

$$\frac{\gamma k_B T v}{\dot{v}\varepsilon} = \gamma\theta_C \tag{7}$$

where θ_C is the growth rate constant, $\dot{v}$ is the rate of volume change with time, that is, $\dot{v} = 4\pi r^2\dot{r}$, where r is particle radius. Applying Equations 6 to 7, dividing both sides by τ_0 and using $t^C_{eff} = \gamma\theta_C$ (Berndt & Muxworthy, 2017) we get

$$\frac{t^C_{eff}}{\tau_0}\ln\left(\frac{t^C_{eff}}{\tau_0}\right) = \frac{v\gamma}{\dot{v}\tau_0} \tag{8}$$

Applying the Lambert W function, $x = W(x)e^{W(x)}$, which to a first order approximates to $W(x) \approx \ln(x) - \ln(\ln(x)) + O(x)$ (Corless et al., 1996), gives the expression for t^C_{eff}:

$$t^C_{eff} = \frac{\gamma v}{\dot{v}}/\ln\left(\frac{v\gamma}{\dot{v}\tau_0}\right) \tag{9}$$

In addition to the gCRM model developed here, we also use a TRM Preisach model (Muxworthy & Heslop, 2011), albeit in a slightly modified form to be consistent with the gCRM model. There are two theoretical differences: (a) we volume normalize the magnetization, and (b) we use the t^T_{eff} as derived by Berndt and Muxworthy (2017). Muxworthy and Heslop (2011) assumed all the particles had equal volume and used t^T_{eff} derived by Borcia et al. (2002), which is one to two orders of magnitude greater than that of Berndt and Muxworthy (2017). The

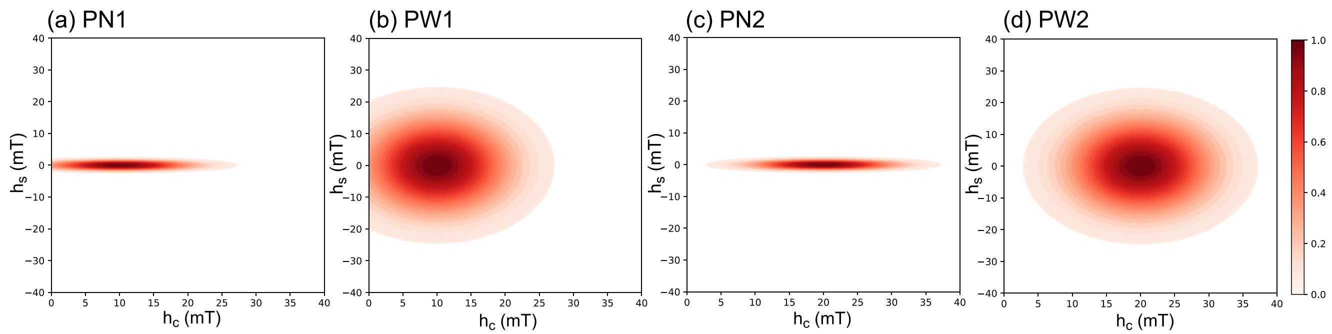

Figure 2. Four end-member Preisach distributions with varying Gaussian distributions in h_c and h_s. The distributions are normalized by the peak of each Preisach distribution. (a) PN1: μ_{h_c}: 10 mT, σ_{h_s}: 1 mT (b) PW1: μ_{h_c}: 10 mT, σ_{h_s}: 10 mT, (c) PN2: μ_{h_c}: 20 mT, σ_{h_s}: 1 mT and (d) PW2: μ_{h_c}: 20 mT, σ_{h_s}: 10 mT. PN and PW distributions have median interaction fields of 0.67 mT and 6.7 mT, equivalent to magnetite concentrations of 2.6% and 21% (Muxworthy & Williams, 2005).

combined effect increases intensities by ∼15%, but the trends are the same. In addition, the TRM Preisach algorithm is a new version of the code written in Python; the previous version was written in Fortran 95 (Muxworthy & Heslop, 2011).

3. Modeling CRM Acquisition of Synthetic Distributions

We model gCRM acquisition for specific magnetic assemblages using synthetic Preisach distributions, which are normally distributed in both h_c and h_s. These can be easily replaced by experimentally measured first-order-reversal-curve (FORC) distributions (e.g., Di Chiara et al., 2017; Muxworthy et al., 2011; Muxworthy et al., 2017) because Preisach and FORC distributions are both plots of h_c and h_s, but FORC diagrams are experimentally derived and not usually symmetrical. The Preisach distributions are populated with a number of hysterons, for example, 5×10^5, each assigned a h_c and h_s value, where $h_c = H_c\sqrt{2}$ (Muxworthy & Heslop, 2011). During remanence acquisition, each hysteron has a statistical alignment with the applied field during blocking, given by Equation 3. This statistical alignment essentially increases the number of modeled particles.

H_c has been proven empirically to be $\propto H_f$ ($\propto 1/v_{act}$, Equation 2) (Barbier, 1954). It has been shown that v_{act} is identical to actual particle volume v for isolated "ideal" SD particles, by $v = v_{\text{act}}/[1 - H/H_k]$ where H is the total external fields (Gaunt, 1986). Using the empirical Barbier relationship allows us to directly populate the Preisach model with a distribution of SW particles with associated volumes. We use $H_c \propto v_{act}^{-0.68}$, determined by Muxworthy et al. (2009) for basaltic rocks. We chose model parameters characteristic of magnetite: M_s of 480 kA/m, a Curie temperature of 578°C, and a Barbier coefficient of 0.68 (Dunlop & Özdemir, 1997; Muxworthy et al., 2009). M_s is well-defined, and the model is insensitive to both the Curie temperature and the Barbier coefficient; gCRM/saturating isothermal remanence (SIRM) varies by 1% for a 10°C change in Curie temperature and 2% for a 10% change in the coefficient. Muxworthy et al. (2011) found a ∼5% change in the TRM/SIRM ratio for a 10% change in the Barbier coefficient.

3.1. Synthetic Preisach Distributions

To investigate how gCRMs vary with magnetic properties we consider four "end-member" Preisach distributions (Figure 2). We vary the mean coercivity μ_{h_c} and the level of magnetostatic interactions by changing the standard deviation σ_{h_s} of the Gaussian distribution in the h_s axis. In FORC analysis, the full-width at half maximum (FWHM) is used to describe the spread of a distribution (Muxworthy & Dunlop, 2002); FWHM ≈ 2.355σ for Gaussian distributions (Weisstein, 2009). We use a weakly interacting case as opposed to a non-interacting as the Preisach model requires a finite width in h_s, this is also representative of FORC diagrams of natural samples which have finite FWHM values (Roberts et al., 2000).

4. gCRM Intensity and Growth Rate

Key to modeling gCRM acquisition is growth rate. Rickard (2019) found pyrite framboids grew over 5 days in nature and in hours in laboratory conditions, and Baumgartner et al. (2013) found timescales on the order of hours for magnetite growth in laboratory conditions. Based on these observations, unless stated, we chose a

10.1029/2022JB025858

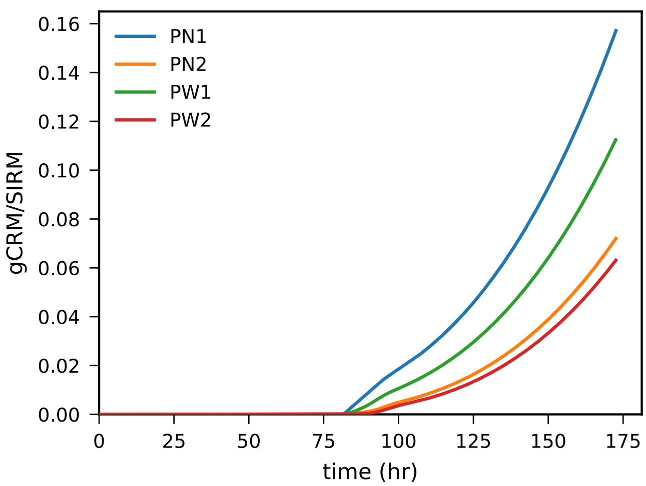

Figure 3. Acquisition of grain-growth chemical remanent magnetization (gCRM) versus time during grain growth for all four Preisach distributions (Figure 2). Simulated gCRM intensity is normalized by simulated saturating isothermal remanence.

growth time of 172 hours, which is of the same order of magnitude as growth times seen in nature and laboratory studies. This corresponds to a growth rate of 10^{-13} m s^{-1}. It is possible that minerals can grow over longer timescales and we have considered this when investigating the effect of growth rate on gCRMs. All the particles in the model have the same growth rate, therefore, time zero is defined as when the largest particle nucleates; smaller particles nucleate at later times. Shcherbakov et al. (2017) also used a constant growth rate on the order of 10^{-13} m s^{-1} in their model which is consistent with their experimental timescales.

In Figure 3 gCRM acquisition is calculated as a function of time for all four Preisach distributions (Figure 2). Magnetizations are normalized by the SIRM following previous studies (Jiang et al., 2015; Muxworthy & Heslop, 2011). The errors in magnetization are <0.1% and not shown in Figure 4 or any subsequent figures. gCRM acquisition curves are similar in shape for all Preisach distributions, only the final intensities and gCRM onset times differing (Figure 3). Initially during growth, there is no remanence as particles are SP. When particles grow through their blocking volume and move into the remanence region (region 4 in Figure 1), a gCRM is acquired. The gCRM continues to grow as particle size increases to their terminal volume. Shifting the Preisach distribution to higher coercivities reduces the final intensities by 54% between PN1 and PN2, and 43% between PW1 and PW2, because higher coercivity particles cross into the remanence region and block at smaller volumes with a lower probability of aligning with the field (Equation 3). The onset of gCRM acquisition is delayed for higher coercivity distributions because the majority of particles are smaller and nucleate later. Our modeled gCRM acquisition curves (Figure 3) are comparable to those predicted by previous Monte Carlo models of gCRM acquisition (Shcherbakov et al., 2017), although Shcherbakov et al. (2017) found a decrease in acquisition rate at intermediate volumes due to viscous magnetization effects. In a test for the linearity of gCRM intensity with applied field, it was found to increase linearly up to 200 μT, in agreement with a linear increase up to 230 μT observed experimentally for magnetite (Pick & Tauxe, 1991). Unless stated, we use a field intensity of 50 μT in the model.

We modeled gCRM acquisition for different growth times and found gCRM/SIRM intensity increases with growth time for all Preisach distributions. When increasing growth times from 1,000 s to 30 kyr the gCRM/SIRM ratio increased by: 87% for PN2, 81% for PW2, 80% for PN1 and 69% for PW1 (Figure 4). Over longer timescales, particles have longer to equilibrate with the applied field, blocking at larger volumes with a higher probability of aligning with the applied field. Blocking at larger volumes also leads to an increase in experienced magnetostatic interactions, which increases the number of field-blocked particles (regions 1 and 2 in Figure 1) and reduces the proportion in the remanence region. This reduces the rate of intensity increase with growth time for strongly interacting systems; this reduction is greater for P1 distributions because lower coercivity particles block at larger volumes. Using a model for non-interacting SD particles, a slightly lower intensity increase of 60% over the same time interval was calculated by McClelland (1996), compared to > 69% found in this study. This difference is due to the different methods of incorporating growth rate: this study uses an effective time, whilst McClelland (1996) uses a single relaxation time.

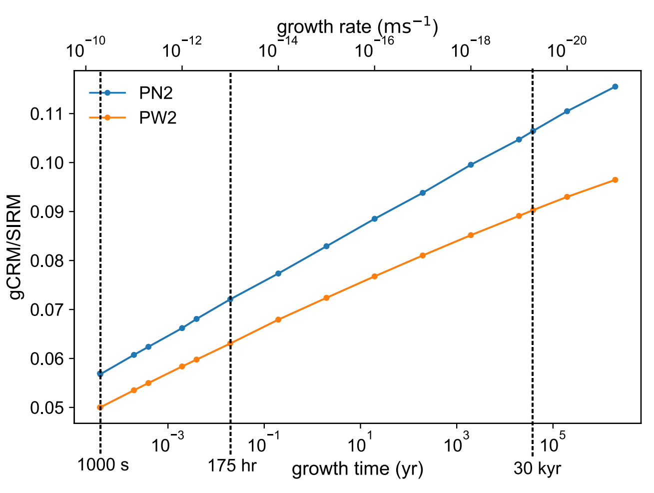

Figure 4. Grain-growth chemical remanent magnetization (gCRM) intensity versus growth rate for Preisach distributions PN2 and PW2. gCRM intensity normalized to SIRM. The standard growth time of 175 hr is highlighted by the dashed line on the graph; this is the growth rate used in the majority of this study. The growth times used in McClelland (1996) are also highlighted. The simulated field intensity was 50 μT.

We compare gCRM recording ability versus TRM as a function of σ_{h_s} for a fixed coercivity distribution (P2) and as a function of μ_{h_c} for a fixed interaction distribution (PN) in Figure 5. Unless stated, we use a standard cooling/heating time of 1 hr in TRM acquisition or simulated laboratory cooling/heating.

gCRMs are more sensitive to the coercivity distribution than TRMs (Figure 5a); the gCRM/SIRM ratio decreases 54% between PN1 and PN2 compared to 24% for the TRM/SIRM ratio. Higher coercivity particles block

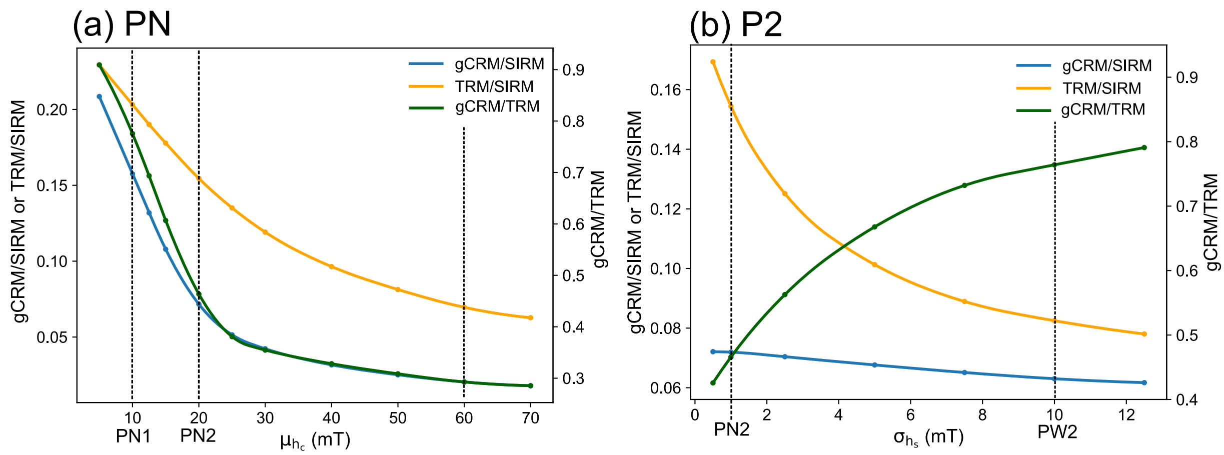

Figure 5. (a) Grain-growth chemical remanent magnetization (gCRM)/saturating isothermal remanence (SIRM), thermoremanent magnetization (TRM)/SIRM intensities and gCRM/TRM ratio versus mean coercivity μ_{h_c}, for Preisach distributions of type PN. PN1, PN2 and the $\mu_{h_c} = 60$ mT used by McClelland (1996) highlighted with black dashed lines. (b) gCRM/SIRM, TRM/SIRM intensities and gCRM/TRM ratio versus distribution width σ_{h_s}, that is, varying levels of magnetostatic interactions, for Preisach distributions of coercivity type P2. PN2 and PW2 distributions highlighted with black dashed lines. Magnetization normalized to the SIRM.

at smaller volumes during gCRM acquisition and at higher temperatures during TRM acquisition. Both of these effects decrease the intensity by reducing the probability of a particle aligning with the applied field during blocking. TRMs are less sensitive to changes in coercivity distribution than gCRMs, because the decrease in field alignment with increased temperature is partly canceled by the temperature dependence of M_s (Equation 3).

gCRM/SIRM and TRM/SIRM both decrease with increasing magnetostatic interactions (Figure 1b). gCRM/SIRM decreases by 12% and TRM/SIRM by 47% between PN2 and PW2. A larger spread in the h_s axis decreases the percentage of the Preisach distribution within the remanence region, that is, region 4 in Figure 1, as more particles are field-blocked, which decreases intensity. This follows expected behavior (Dunlop, 1969). Blocking volumes during room-temperature gCRM acquisition are ~4% of those during TRM acquisition for the same input Preisach distribution. As $h_s \propto v$, the level of interactions experienced during gCRM acquisition is significantly less than during TRM acquisition, reducing the effect of interactions on gCRM intensity compared to TRM. A decrease in gCRM intensity with increased interactions was also seen in Monte Carlo models (Shcherbakov et al., 1996, 2017).

5. Simulated Thermal Demagnetization of gCRMs

We simulated thermal demagnetization of gCRM (initial state $gCRM_0$) and TRM states (initial state TRM_0) in Preisach space (Figure 6). gCRMs unblock more rapidly upon heating than TRMs. Increasing coercivity shifts the unblocking spectra for gCRM and TRM to higher temperatures as expected. Increasing interactions causes the gCRM and TRM curves to diverge, that is, PN2 versus PW2 (Figure 6). In the TRM case, increasing interactions pushes the unblocking spectra to slightly higher temperatures, because the particles which block and unblock at lower temperatures experience the highest interactions and do not carry a remanence in the Preisach model. The gCRM spectra shifts to lower temperatures with increased interactions because volumes and interactions are smaller during gCRM acquisition than during thermal demagnetization, and particles unblocking at lower temperatures carry a remanence. The impact of interactions on gCRM and TRM thermal demagnetization curves is greater for the lower coercivity distributions, that is, PN1 and PW1 versus PN2 and PW2, where blocking/unblocking temperatures are lower.

The lower thermal stability of gCRMs relative to TRMs is consistent with previous theoretical studies of non-interacting and interacting assemblages (McClelland, 1996; Shcherbakov & Sycheva, 2019; Shcherbakov et al., 1996, 2017, 2021). In contrast to this study, Shcherbakov et al. (1996) found increasing interactions pushes both gCRM and TRM unblocking spectra to higher temperatures. In their model, Shcherbakov et al. (1996) included dynamic magnetic interactions involving SP grains in addition to the magnetostatic interactions used in this Preisach model. It is known that dynamic interactions between highly interact-

10.1029/2022JB025858

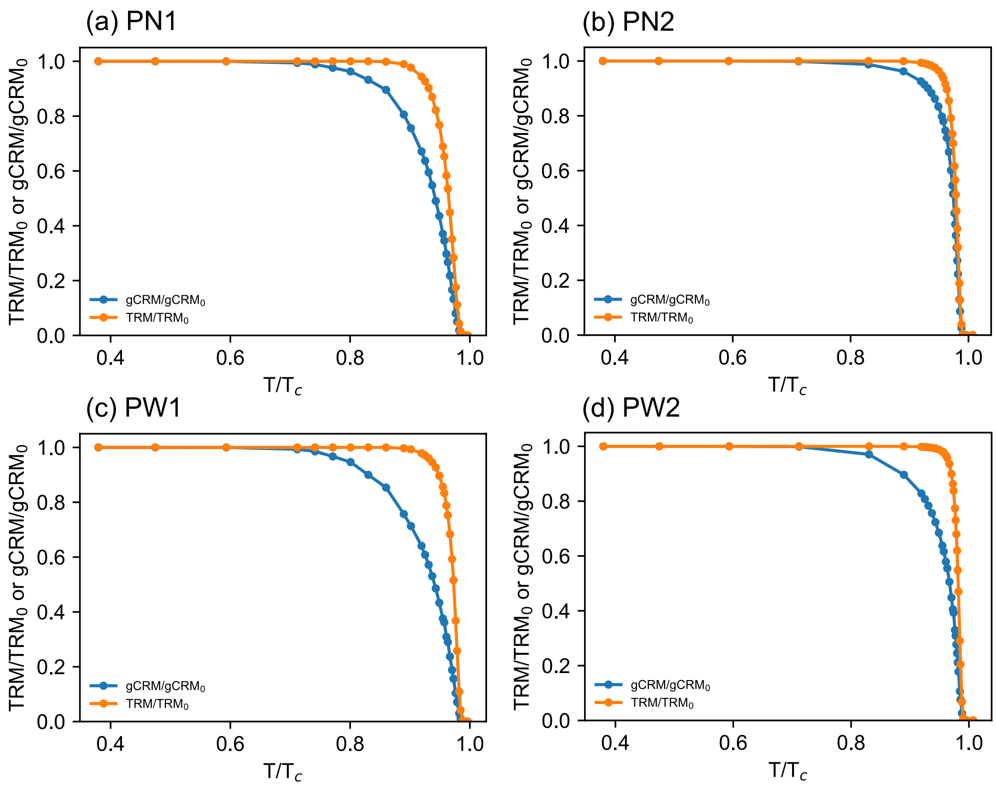

Figure 6. Simulated thermal demagnetization spectra for both grain-growth chemical remanent magnetization (gCRMs) (initial state $gCRM_0$) and thermoremanent magnetization (TRMs) (initial state TRM_0) induced in the four end-member Preisach distributions (Figure 2): (a) PN1, (b) PN2, (c) PW1 and (d) PW2. The remanent magnetizations are normalized to $gCRM_0$ and TRM_0. The simulated field intensity was 50 μT, and the simulated heating time was 1 hr.

ing SP particles can lead to spin-glass states which increases unblocking temperature (Wohlfarth, 1979); however, concentrations in natural systems tend to be low (≪10%) and the system is considered only weakly interacting, which leads to the opposite relationship, that is, a slight decrease in blocking temperature with interactions (Jönsson, 2003). It would appear therefore, that the highly interacting regime of Shcherbakov et al. (1996) captured the response of a spin-glass system, which is not thought to be generally applicable to rocks.

6. gCRM Behavior During the Thellier Paleointensity Protocol

We simulated the Thellier-Thellier-Coe paleointensity protocol (Coe, 1967; Thellier & Thellier, 1959), for gCRMs and TRMs for the four end-member Preisach distributions (Figures 2 and 7); the latter for comparison. We consider gCRMs acquired at a range of temperatures, and a simple model for TCRM: a gCRM acquired at high temperature with cooling in the same field. Unless stated the simulated laboratory field was the same intensity and direction as the simulated acquisition field.

6.1. gCRM Induced at Room Temperature

The simulated Arai plots for the gCRM are concave-up for all Preisach distributions (Figure 7). A large proportion of the gCRM is lost at low temperatures during simulated heating because the majority of a gCRM is carried by low coercivity particles, whereas the majority of the pTRM is carried by higher coercivity particles with higher blocking temperatures. This effect increases the degree of curvature for lower coercivity distributions, for example, PN2 to PN1 (Figure 7). Curvature increases between PN- and PW-type distributions because of the opposing affect interactions have on the gCRM and TRM blocking spectra. This reduces the unblocking temperature of the gCRM and increases the temperature pTRM is gained. The concave-up shape is in agreement with previous models for gCRMs (McClelland, 1996; Shcherbakov & Sycheva, 2019; Shcherbakov et al., 2017, 2021).

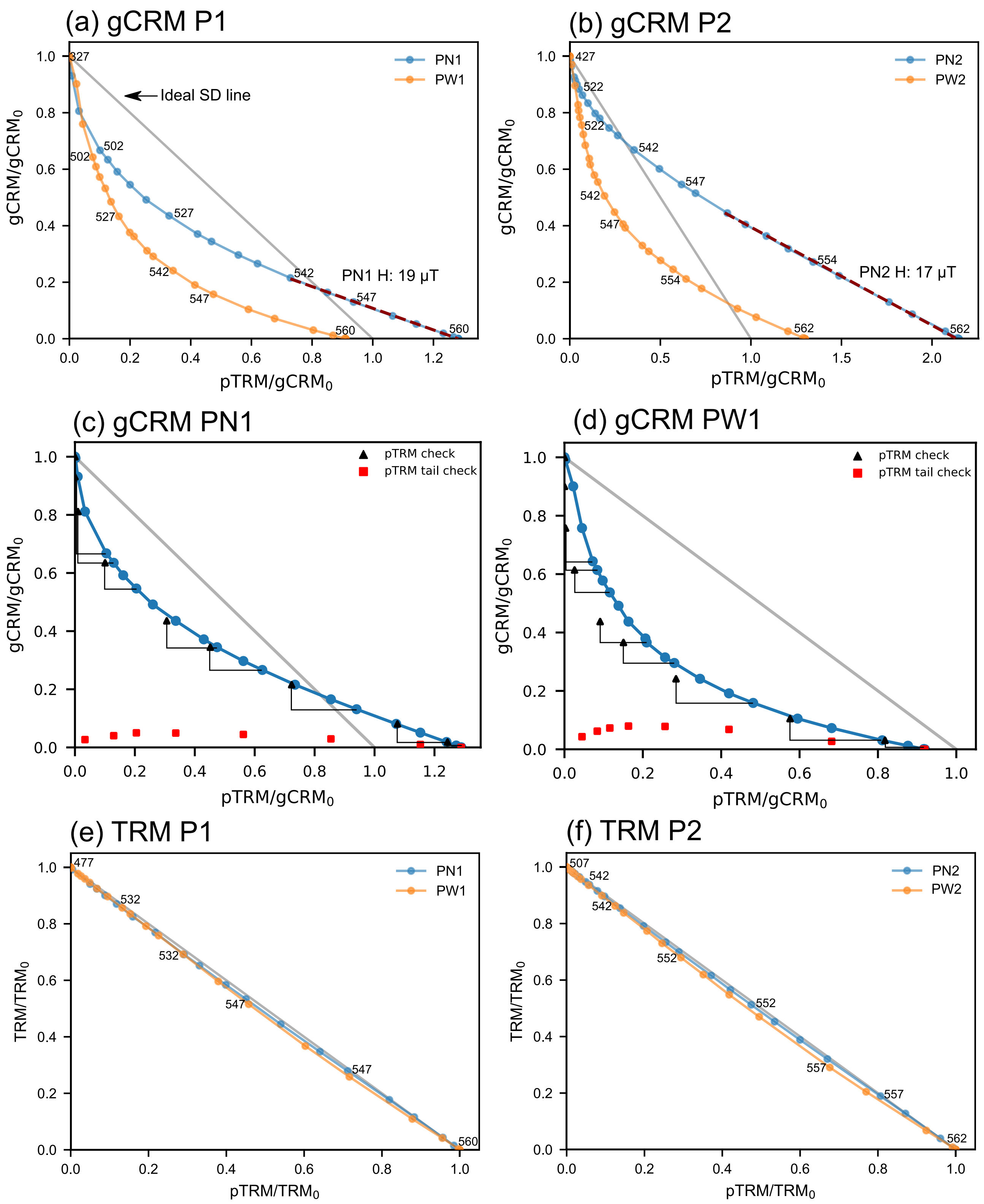

(a) gCRM P1
gCRM/gCRM$_0$
pTRM/gCRM$_0$
Ideal SD line
PN1
PW1
PN1 H: 19 μT
327
502
527
542
547
560
(b) gCRM P2
PN2
PW2
PN2 H: 17 μT
427
522
542
547
554
562
(c) gCRM PN1
pTRM check
pTRM tail check
(d) gCRM PW1
(e) TRM P1
TRM/TRM$_0$
pTRM/TRM$_0$
477
532
547
560
(f) TRM P2
507
542
552
557
562

Figure 7.

The gCRM Arai plots have two approximately linear regions at low and high temperatures (Figure 7); these are commonly interpreted in paleointensity estimations (e.g., Tanaka & Yamamoto, 2016). We make paleointensity estimates using these regions for the four Preisach distributions using the modified-TTB selection criteria (Paterson et al., 2014), which is: (a) number of points in section ($n > 5$), (b) normalized standard error of the slope ($\beta < 0.15$), (c) fraction of remanent magnetization ($f > 0.35$), (d) maximum difference produced by a pTRM check, normalized by the $gCRM_0$ or TRM_0 (δ(CK) < 9), (e) a measure of the cumulative alteration (δ(pal) < 18), and (f) maximum difference produced by a pTRM-tail check normalized by the $gCRM_0$ or TRM_0 (δ(TR) < 20). We also calculated the degree of curvature, defined as the inverse of the radius of the best fit circle of the selected section ($\bar{k}' < 0.27$) (Paterson et al., 2014). The accepted fit with the maximum quality factor q was chosen. Only fits for the high-temperature sections of the weakly interacting Preisach distributions passed the criteria and paleointensity estimates of 19 and 17 μT were made for PN1 and PN2 respectively.

The pTRM checks plot to the left, for the same reason the Arai plots are concave-up, that is, the gCRM is removed at lower temperatures than the pTRM is gained, see Figures 7c and 7d for P1 and Figures 8d and 8g for P2. This effect and the magnitude of pTRM checks are reduced at higher temperatures. The pTRM-tail checks are positive due to the in-field unblocking and reblocking of positively magnetized particles during the pTRM step; this is due to the shifting of the thermal critical barriers by $+h_a$ during in-field steps (Figure 1). These particles experience the largest magnetostatic interactions during reheating and are aligned close to the applied field during simulated pTRM acquisition, but not during gCRM acquisition where interactions are smaller. The magnitude of pTRM and pTRM-tail checks are larger for strongly interacting distributions as the differences between gCRM and pTRM intensities increase.

The high-temperature fits for the weakly interacting distributions PN1 and PN2 underestimate the inducing field by 62% and 66% respectively. gCRM Arai plots calculated by McClelland (1996) for a higher coercivity (60 mT) non-interacting system also found an approximately linear high-temperature section which underestimated the inducing field by 60%. This result along with our two estimates suggests that paleointensity estimates from high-temperature segments for weakly/non-interacting systems are independent of coercivity and typically underestimate the field by ∼60%.

The simulated TRM Arai plots are more linear than the gCRM plots (Figures 7e and 7f). However, there is still some concave-up curvature in the TRM Arai plots. This reflects the fact that pTRM gained at intermediate temperature steps is less than the TRM lost. This is an artifact in the model due the use of discrete temperature steps.

As expected, $\bar{k}'$ is larger for PW distributions than the PN distributions, but is below the critical value of 0.164 (Paterson, 2011). This low level of curvature is nonetheless significant, and can lead to differences in paleointensity estimates of up to 5% for PN and 8% for PW distributions, depending on the temperature range used.

Increasing the growth time steepens the Arai plots across the whole temperature spectrum (Figures 9a and 9b) and increases the paleointensity estimates. This steepening is less pronounced in the strongly interacting regime, for example, PW2, because interactions moderate the effect of growth time on gCRM intensity (Figure 4). In their model for non-interacting SD assemblages, McClelland (1996) found the same trends between growth time and intensity as we found for PN2 (Figure 9a).

The simulated TRM Arai plots are less sensitive to cooling rate than gCRMs are to growth rate (Figure 9). The TRM Arai plots for PN2 and PW2 display different responses to cooling time. In the PN2 case, increasing the cooling time increases TRM_0, which reduces the pTRM/TRM_0 ratio. The opposite response is seen for the PW2 case, TRM_0 decreases with increased cooling time.

For the weakly interacting distributions PN1 and PN2 (Figure 9c), TRM intensities increase with cooling time because particles have longer to equilibrate and block at lower temperatures with an increased probability of

Figure 7. Arai plots for: (a) grain-growth chemical remanent magnetization (gCRM) induced in Preisach distributions PN1 and PW1, (b) gCRM induced in PN2 and PW2, (e) thermoremanent magnetization (TRM) induced in PN1 and PW1, and (f) TRM induced in PN2 and PW2. $gCRM_0$ or TRM_0 is the initial magnetization. Accepted paleointensity estimates were made for the high-temperature (H) linear segments in the PN1 and PN2 gCRM Arai plots in (a) and (b). The paleointensity estimates were made using Paleointensity.org using the modified TTB criteria, $\bar{k}'$ and maximizing the q value. Least-square fits of the accepted segments are shown in red. The errors on paleointensity estimates are below 10% and shown in Table 1. The gray line displays ideal TRM behavior according to non-interacting SD theory (Néel, 1949). pTRM checks and pTRM-tail checks were calculated and are shown in (c) and (d) for P1 distributions and in Figure 8 for P2 distributions. Magnetizations are normalized to the initial magnetization.

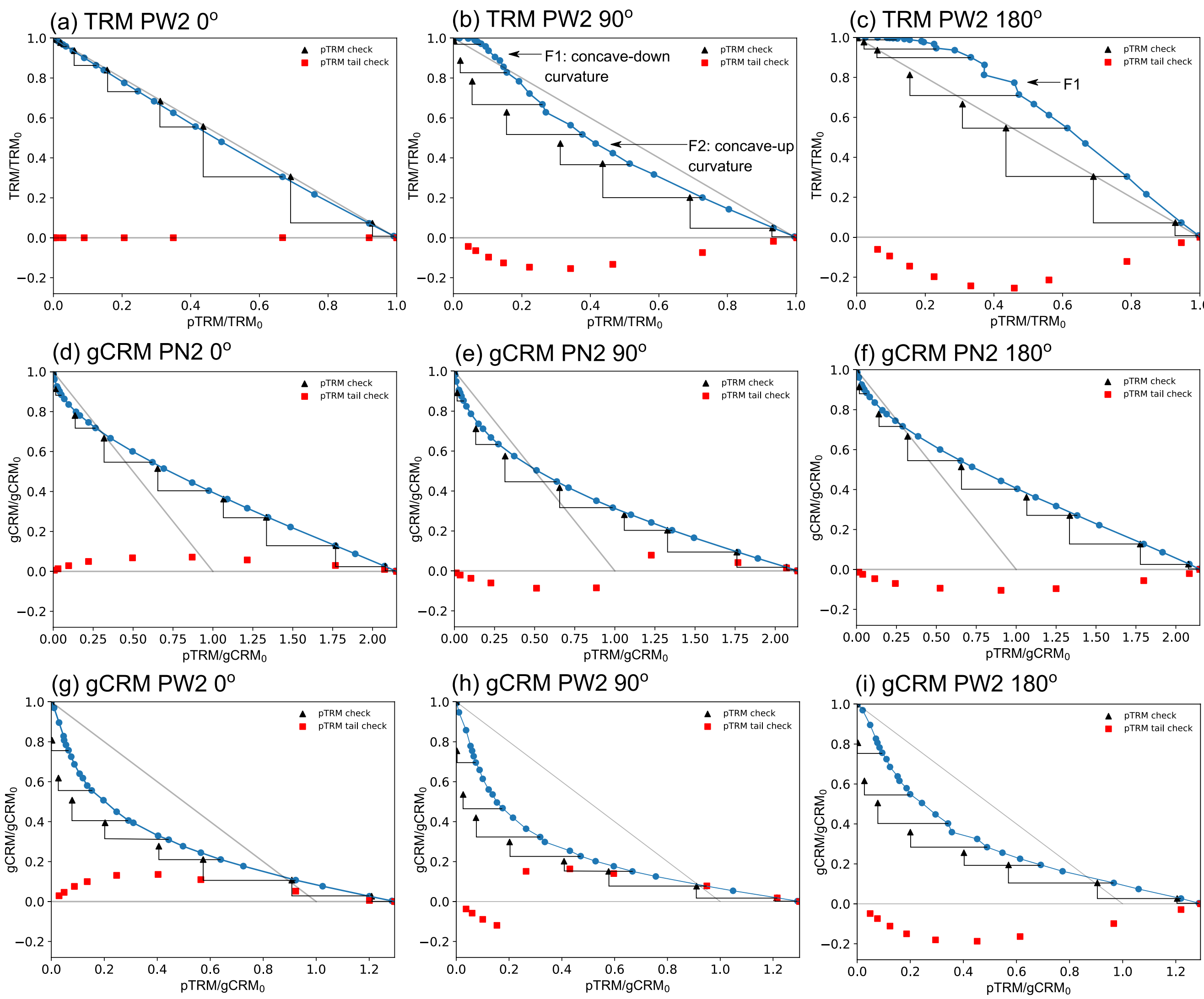

Figure 8. Arai plots with partial thermoremanent magnetization (pTRM) checks and pTRM-tail checks for TRM induced in PW2, and grain-growth chemical remanent magnetization (gCRM) induced in PN2 and PW2 (Figure 2) with varying angular difference between the TRM or gCRM acquisition field and the simulated laboratory field: (a) TRM in PW2 at 0°, (b) TRM in PW2 at 90°, (c) TRM in PW2 at 180°, (d) gCRM in PN2 at 0°, (e) gCRM in PN2 at 90° (f) gCRM in PN2 at 180°, (g) gCRM in PW2 at 0°, (h) gCRM in PW2 at 90° and (i) gCRM in PW2 at 180°. Two features (F1 and F2) are highlighted in the TRM Arai plots in (b) and (c): F1 is a concave-down curvature at low temperature in (b) and across all temperatures in (c) and F2 is concave-up curvature at high temperature in (b). The simulated field was 50 μT at all times. The gray line represents ideal SD behavior.

field alignment (Dodson & McClelland-Brown, 1980). For the strongly interacting systems PW1 and PW2 (Figure 9d), the opposite trend is found. TRM intensities decrease with cooling time because particles blocking at lower temperatures experience stronger interactions as h_s varies with M_s, which reduces the number of particles in the remanence region (Muxworthy & Heslop, 2011).

In the literature, slow-cooled non-interacting SD assemblages are consistently found to overestimate paleointensity, both theoretically (e.g., Dodson & McClelland-Brown, 1980; Halgedahl et al., 1980; Shcherbakov et al., 2021) and experimentally (e.g., Ferk et al., 2014). Theoretical predictions predict a 5%–7% intensity increase per order of magnitude increase in the cooling time (Dodson & McClelland-Brown, 1980; Halgedahl et al., 1980; Shcherbakov et al., 2021), in agreement with experimental estimates of 4%–8% (Ferk et al., 2014). We found an increase of only 4% for the weakly interacting case PN2 and 1% for PN1.

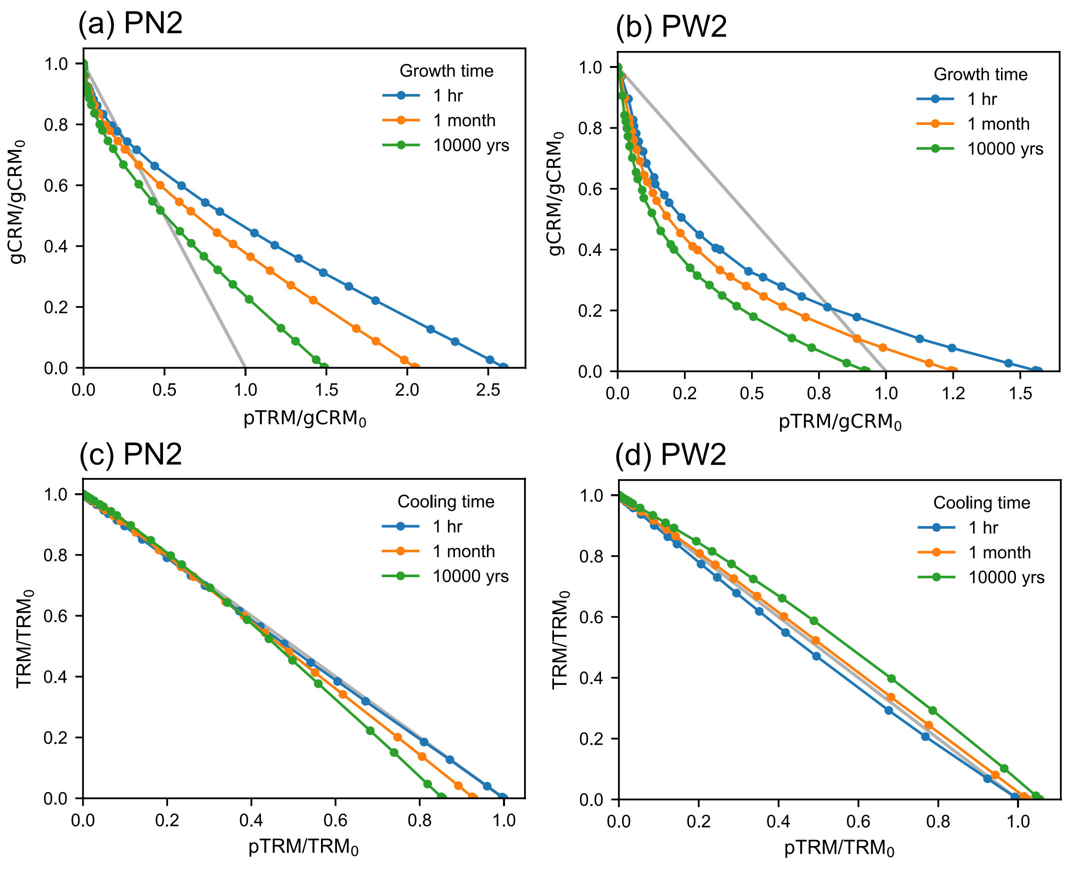

Figure 9. Arai plots for grain-growth chemical remanent magnetization (gCRMs) and thermoremanent magnetization (TRMs) acquired over different growth/cooling times: (a) gCRM in PN2, (b) gCRM in PW2, (c) TRM in PN2 and (d) TRM in PW2. $gCRM_0$ or TRM_0 is the initial magnetization. Magnetizations are normalized by the initial magnetization. The gray line is the TRM Arai plot for an ideal non-interacting SD system with an TRM acquisition time of 1 hr. The simulated acquisition and laboratory field was 50 μT and in the same direction.

6.2. High-Temperature gCRM(T) and TCRM

We modeled high-temperature gCRM(T) and a simple case of TCRM acquisition. In the former, the gCRM was acquired at high temperature, with simulated cooling in zero-field, and in the latter, cooling was in the same field (Figure 10). This is the same approach as used by Shcherbakov et al. (2017).

Arai plots for both gCRM(T) and TCRMs (Figure 10) display little difference between the two acquisition mechanisms except for the acquisition at 527°C. At lower temperatures, that is, <527°C, gCRM(T) and TCRM Arai plots are similar at each temperature because the majority of the magnetization is acquired during high-temperature grain growth. A plateau arises in the gCRM(T) Arai plots in the 527°C case, because this is above the blocking temperature of a significant proportion of the particles. These particles do not acquire a non-zero magnetization during cooling in zero field, but they do acquire a pTRM during the lower temperature in-field steps with no gCRM being removed, that is, this is in part an artifact of simulating zero-field cooling during simulated gCRM(T) acquisition. In the TCRM model these particles only acquire a remanence on simulated cooling.

The linearity of the Arai plots increases with both gCRM(T) and TCRM acquisition temperature between 27°C and 427°C; $\bar{k}'$ decreases from 0.43 to 0.31 for PN2 and from 0.92 to 0.66 for PW2. This is because particles block at temperatures closer to that of a TRM. gCRM(T) and TCRM intensity increases with gCRM(T) acquisition temperature, by 60% and 30% for PN2 and PW2 between 27°C and 427°C. Increasing gCRM(T) acquisition temperature widens the thermal critical barriers for a given time and volume (Figure 1), leading to larger blocking volumes and a relative increase in intensity. This effect is reduced for strongly interacting systems because interactions increase with blocking volumes, which increases the proportion of field-blocked particles. This increase

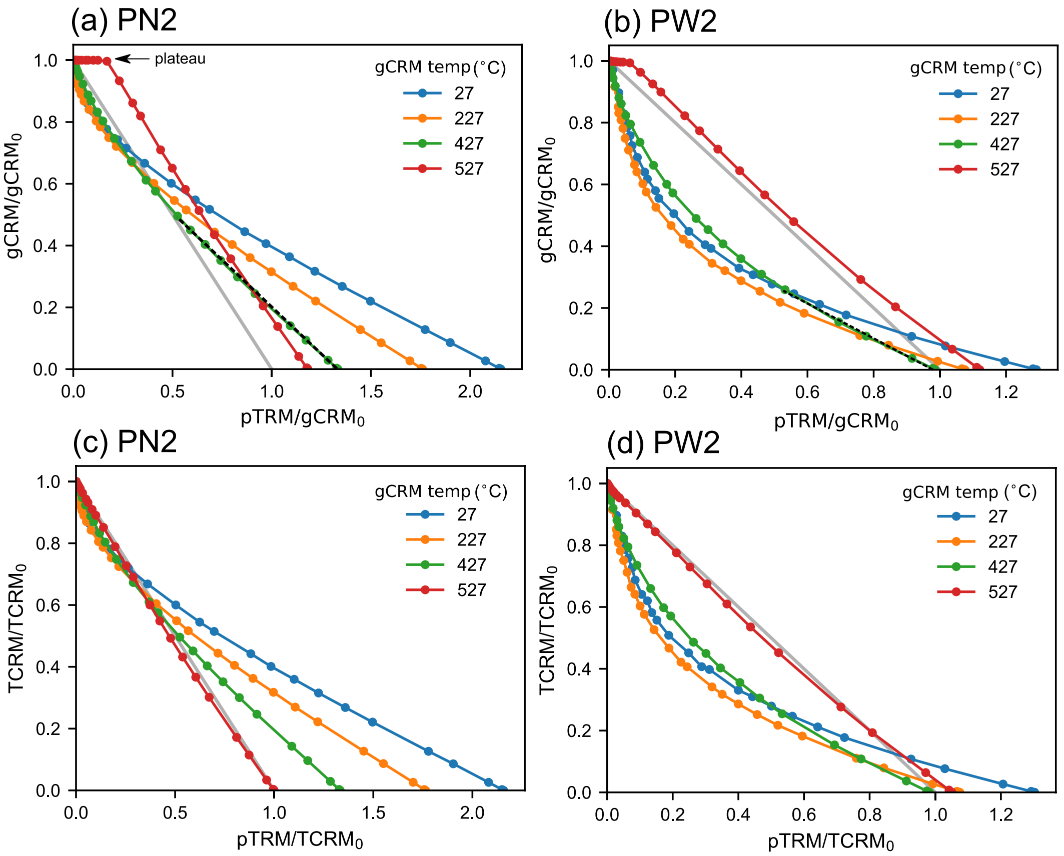

Figure 10. Arai plots for grain-growth chemical remanent magnetization (gCRM)(*T*) and thermochemical remanent magnetization (TCRMs) acquired at 27°C, 227°C, 427°C, and 527°C for: (a) gCRM(*T*) in PN2, (b) gCRM(*T*) in PW2, (c) TCRM in PN2, and (d) TCRM in PW2. The gray line displays ideal thermoremanent magnetization (TRM) behavior. pTRM checks and pTRM-tail checks were carried out and discussed in text. The plateau seen at 527°C labeled in (a). For the 427°C gCRMs, best fit lines have been added to the high temperature sections. Magnetizations are normalized by the initial magnetization. The simulated acquisition field was 50 μT. The simulated laboratory field was the same intensity and in the same direction as the simulated acquisition field.

Table 1
Accepted Paleointensity (PI) Estimates for the High-Temperature Segments of the PN1 and PN2 gCRM Arai Plots Shown in Figures 7a and 7b, the PN2 and PW2 High Temperature gCRM (gCRM(T)) Arai Plots for the 427°C Case Shown in Figures 10a and 10b and the PN1, PN2, PW1 and PW2 TRM Arai Plots Shown in Figures 7e and 7f

Arai plot	PI (μT)	Temp range (°C)	n	f	β	δ(CK)	δ(pal)	δ(TR)	q	$\bar{k}'$
gCRM PN1	19 ± 0.1	540–570	11	0.43	0.007	2.3	1.7	10	55	−0.26
gCRM PN2	17 ± 0.1	550–576	13	0.60	0.005	1.9	1.4	9.8	100	0.047
gCRM(427°C) PN2	31 ± 0.1	548–576	14	0.70	0.009	0.6	0.7	3.6	71	0.09
gCRM(427°C) PW2	31 ± 0.1	552–576	11	0.67	0.024	4.7	3	10	23	0.23
TRM PN1	50 ± 0.1	427–564	22	1.0	0.003	2.1	9.6	0	270	0.041
TRM PN2	50 ± 0.1	507–564	24	1.0	0.003	2.0	11	0	310	0.037
TRM PW1	50 ± 0.3	477–564	27	1.0	0.005	2.5	8.5	0.1	190	0.074
TRM PW2	50 ± 0.4	517–567	23	1.0	0.007	2.6	12	0.3	130	0.094

Note. The columns 3 to 11 are: temp range is the temperature range of the estimate, n is the number of points in section, f is the fraction of remanent magnetization, β is the normalized standard error of the slope, δ(CK) is the maximum normalized difference produced by a pTRM check, δ(pal) is a measure of the cumulative alteration, δ(TR) is the maximum normalized difference produced by a pTRM-tail check, q is the quality factor and $\bar{k}'$ is the degree of curvature. PI estimates were picked and accepted using the modified-TTB protocol and $\bar{k}'$ parameter. The accepted estimate with the highest q factor was used. The inducing field was 50 μT.

in gCRM(T) intensity with acquisition temperature is in agreement with previous studies (Draeger et al., 2006; Shcherbakov et al., 2017).

The gradients of the near-linear high-temperature segments of the gCRM(T) and TCRM Arai plots steepen with acquisition temperature, and the statistics for the pTRM checks and pTRM-tail checks improve. These high-temperature sections pass the modified-TTB selection criteria at 227°C, 427°C, and 527°C for PN2 and at 427°C and 527°C for PW2. Increasing acquisition temperature yields paleointensity estimates closer to the simulated applied field, for example, for 427°C model PI estimates are 30 μT for PN2 and 30 μT for PW2 (Table 1), compared to an expected value of 50 μT; underestimates of 38% and 40% respectively (Figure 10 and Table 1). For the 27°C model, PN2 yields an underestimation of 64%. More segments pass selection criteria at higher temperatures, increasing the risk of incorrect interpretations of incorrect PIs by misinterpreting gCRMs as TRMs. Shcherbakov et al. (2017) found the high temperature portions of Arai plots for high-temperature gCRM(T) grown at 400°C underestimated the applied field by ∼60%–70% for the gCRM(T) case.

6.3. Influence of the Applied Field Angle on Arai Plots

We varied the field angle between the initial gCRM or TRM acquisition direction and the simulated laboratory TRM (ϕ_f). In the model, each particle is initially assigned a random easy-axis. The angle between the easy-axis and the applied field is used to calculate the position of energy barriers during gCRM or TRM acquisition. When the field angle is changed during simulated Thellier analysis, a new angle is calculated. Changing the field angle introduces curvature in the TRM Arai plots, shown for PW2 in Figures 8a–8c. Increasing ϕ_f from 0° to 90° produces concave-down curvature at low temperatures, feature 1 (F1) in Figure 8b, and concave-up curvature at high temperatures, feature 2 (F2) in Figure 8b. Further increasing ϕ_f to 180° produces concave-down curvature (F1) across the whole temperature range (Figure 8c). PTRM checks plot at lower values and pTRM-tails become negative with increasing ϕ_f. To a lesser extent the same trends are found for the PN2 Preisach distribution.

F1 in Figure 8 arises because pTRM gained is larger than TRM removed. During the in-field pTRM acquisition step, the field-bias in the simulated laboratory field direction unblocks and remagnetizes a portion of positively magnetized particles in the simulated laboratory field direction which do not unblock during the zero-field step. This is because the thermal critical barriers are shifted by $+h_a$ in the h_s-axis (Figure 1) for the in-field pTRM acquisition step. This effect increases with interactions and at relatively steeper field angles.

F2 in Figure 8 is caused by the angular dependency of the thermal critical barriers. For particles with the same properties, for example, h_k and h_s, the energy barriers are at a minimum when the angle between the uniaxial easy-axis and field-axis is 0° and 90° and at a maximum at 45° (equation 11 in Muxworthy & Heslop, 2011). Therefore, particles with easy-axes close to 0° and 90° away from the laboratory field will unblock and re-block first at lower temperatures. Due to the distribution of angles about an axis on a sphere, more particles will unblock with angles close to 90° than 0°. These 90° particles are not closely aligned to the simulated laboratory field direction, which reduces the pTRM gained compared to the original TRM lost because they will not be 90° away from the original field direction. In the 180° case, the F1 feature occurs throughout the temperature range because the angle between the easy-axis and field direction is the same during TRM and pTRM acquisition, and the mechanism that causes F2 has no impact.

PTRM checks plot at lower values than the original pTRM, because the field-bias responsible for F1 is not present during the pTRM check as the particles responsible for F1 are demagnetized at higher temperatures. PTRM-tail checks are negative because the particles responsible for F1 which are remagnetized in the simulated laboratory field direction, are not unblocked during the repeated zero-field heating step. This reduces the magnetization at the second zero-field heating step. The pTRM-tail checks are greatest when the angular difference is at 180°.

The influence of ϕ_f on the TRM Arai plot is lower for the PN2 distribution compared to the PW2 distribution, and the PI estimates for PN2 pass the TTB criteria regardless of ϕ_f (Figure 8). In contrast the PW2 distribution fails the TTB selection criteria at 90° or 180° for PW2. This highlights the importance of minimizing the angular difference between natural remanent magnetization (NRM) and laboratory field directions during paleointensity determination (e.g., Kono, 1974; Yu et al., 2004).

Shcherbakov et al. (2021) previously showed that pTRM gained exceeds the TRM lost at 180° for an individual temperature step in a Thellier-Thellier-Coe-type protocol. In their study they analytically solved the master equation for non-interacting single-coercivity SD particles. However, when they determined Arai plots for the 90° case, they did not observe the F1 and F2 structure that we did (Figure 8b). This is because they did not consider a distribution of easy axis orientations, as is done in this study. Shcherbakov et al. (2021) only considered distributions of aligned particles. It is the distribution of orientations that gives rise to the behavior seen in Figure 8b.

The effect of varying ϕ_f on the gCRM Arai plots is shown in Figures 8d–8f for the PN2 distribution and Figures 8g–8i for PW2. The gCRM Arai-plot behavior are the result of F1 and F2 being superimposed on the already concave-up gCRM Arai plots. For example, increasing ϕ_f to 90° increases the concave-up curvature, and further increasing ϕ_f to 180° decreases the concave-up curvature. Increasing ϕ_f also causes the pTRM-tail checks to become negative as seen in the TRM Arai plots.

7. Discussion

Our Preisach model has shown that gCRM behavior including gCRM intensity is strongly dependent on coercivity distribution, the mean magnetostatic interaction field distribution of a sample, and acquisition conditions, for example, temperature and growth rate (Figures 4, 5 and 10). Increasing the coercivity distribution decreases gCRM intensity, as does increasing magnetostatic interactions (Figure 5). Increasing the growth time or temperature during gCRM acquisition increases gCRM intensity. Models of gCRM behavior during Thellier-Thellier-Coe protocol simulation found the gCRM Arai plots are often dominated by concave-up curvature (Figures 7–10). This concave-up curvature is less pronounced for weakly magnetostatically interacting distributions. Arai plots for gCRMs can still pass standard selection criteria, that is, the modified-TTB criteria of Paterson et al. (2014), though the paleointensity estimates are usually too low (Table 1). Now we will discuss each of the mechanisms that control gCRM intensity, and the implications of our model for paleointensity determination. We will also make some remarks on the angular dependence of TRM.

7.1. Mechanisms Controlling gCRM Intensity

Varying the coercivity distribution and gCRM acquisition conditions influence particle blocking volumes. Increasing the blocking volume of a particle increases the probability of its magnetization being aligned with the applied field, this increases gCRM intensity. Higher coercivity particles block at smaller volumes, therefore higher coercivity Preisach distributions, for example, P2 versus P1, have lower gCRM intensities (Figure 5a). Decreasing the growth rate during gCRM acquisition increases the time available for particles to equilibrate with the applied field, so particles block later during growth at larger volumes. Increasing gCRM acquisition temperature also increases blocking volumes by expanding the thermal critical curves for each time and volume step. Both these effects increase gCRM intensity (Figures 4 and 10). Conversely, increasing magnetostatic interactions increases the number of field-blocked particles and reduces the number of particles in the remanence region, which decreases gCRM intensity (Figure 5b).

In contrast to gCRM, TRM intensity is controlled by blocking temperature. Increasing a particles blocking temperature reduces the probability of alignment between a particles magnetization and the applied field, decreasing TRM intensity. This decrease in field alignment and TRM intensity is moderated by the temperature dependence of M_s (Equation 3). This results in TRMs being less sensitive than gCRMs to both sample behavior, for example, coercivity distribution, and blocking environment, for example, acquisition rate (Figures 5a and 9). However, TRMs are more sensitive to variations in magnetostatic interactions than gCRMs because the particles are fully grown during TRM acquisition and $h_s \propto v$. Thus the gCRM/TRM ratio increases with increasing magnetostatic interactions (Figure 5b).

Our Preisach model displays the same major trends in gCRM intensity as in previously published models based on theoretical studies of non- and interacting SD systems (e.g., McClelland, 1996; Shcherbakov et al., 1996, 2017). We found gCRM intensity increases with growth time in agreement with calculations for non-interacting systems by McClelland (1996) and with acquisition temperature for non- and interacting systems (Shcherbakov et al., 2017). Furthermore, our modeled reduction in gCRM intensity with increasing interactions is consistent with calculations by Shcherbakov et al. (2017). However, there are differences between our model and previous models: the specific gCRM intensities and gCRM/TRM ratios differ, primarily, because our model incorporates growth rate and interactions differently. Our model incorporates growth rate using a derived effective relaxation time (Equation 9) which evolves with time and volume during gCRM acquisition; previous models used a constant relaxation time (McClelland, 1996; Shcherbakov et al., 2017). The use of Equation 9 for the effective time, increases the sensitivity of gCRM intensity with respect to growth rate by ∼10% compared to previous models (McClelland, 1996).

It is important to determine how our modeled intensities compare to experimental data. Despite numerous experimental studies of gCRMs in various magnetic minerals at a range of temperatures (e.g., Hoye & Evans, 1975; Jiang et al., 2015; Nguyen & Pechersky, 1987; Pick & Tauxe, 1991; Stokking & Tauxe, 1990; Özdemir & Dunlop, 1993), the studies which can be directly compared to are limited. This is due to type transitions between multiple magnetic phases, that is, not "true" gCRMs, and lack of comparable measurements, for example, SIRM or TRM intensity (e.g., Nguyen & Pechersky, 1987; Pick & Tauxe, 1991). To compare with suitable experimental data (i.e., Hoye & Evans, 1975; Stokking & Tauxe, 1990; Özdemir & Dunlop, 1993), we consider gCRM/SIRM, gCRM(T)/SIRM and gCRM/TRM ratios. Özdemir and Dunlop (1993) measured gCRM(250°C)/SIRM ≈ 0.07 for gCRMs acquired when paramagnetic lepidocrocite alters to maghemite. We modeled assemblages of maghemite particles with a Curie temperature of 645°C (Özdemir & Banerjee, 1984) and a saturation magnetization of 380 kA/m, and found gCRM(250°C)/SIRM ratios of 0.087 for PN2 and 0.077 for PW2. Our modeled ratios are higher, which is likely due to uncertainties in the input Preisach distribution which was not measured by Özdemir and Dunlop (1993).

Our model predicted gCRM/TRM ratios in the range 0.28–1.2 for various grain distributions, acquisition times (1,000 s –10,000 years) and temperatures (27°C–527°C). gCRM(527°C)/TRM ratios of 0.85 and 0.89 for PN2 and PW2 were calculated from the Aria plots and a maximum gCRM/TRM of 1.2 was found for gCRMs acquired over 10,000 years relative to TRMs acquired on laboratory timescales (Figures 4, 5 and 10). A large variation in gCRM/TRM ratios has also been reported experimentally: Stokking and Tauxe (1990) found gCRM/TRM ≈ 0.15 acquired in hematite at 97°C, whereas Hoye and Evans (1975) measured gCRM/TRM ≈ 0.6 for magnetite formation from oxidation of olivine at 500°C, by measuring anhysteretic remanent magnetzation (ARM) and using TRM = 1.2ARM. Our model, by comparison, predicted gCRM(527°C)/TRM of 0.84 and 0.90 for PN2 and PW2. Gendler et al. (2005) measured a gCRM(350°C)/TRM of 0.9 for maghemite formed from lepidocrocite, we calculated gCRM(350°C)/TRMs of 0.65 and 1.08 for PN2 and PW2 using the maghemite parameters. These experimental ratios are generally lower than our model predicts. This may be attributed to our Preisach model modeling magnetite and maghemite particles using synthetic coercivity distributions or alteration during gCRM or TRM acquisition in experimental studies. All previous theoretical gCRM studies have modeled lower ratios than seen experimentally (McClelland, 1996; Shcherbakov et al., 1996), which could be caused by non-SD behavior or the models not capturing the experimental cases accurately. In our case, we have estimated the input Preisach distribution.

7.2. gCRM Contribution to Paleointensity Determination

A key aim of this study was to determine if gCRMs can be identified on Arai plots and whether their behavior passes current acceptance criteria (Paterson et al., 2014). All the gCRM Arai plots were concave-up (Figure 7). This concave-up shape is distinctive, but not unique to gCRMs as there are other mechanisms known to cause this concave-up behavior, for example, multidomain (MD) grains (e.g., Levi, 1977), the aging of the samples between TRM acquisition and measurement (Shaar & Tauxe, 2015), chemical alteration (Kosterov & Prévot, 1998) and angular variations between acquisition and laboratory field (Xu & Dunlop, 2004). Another key distinguishing feature is the pTRM checks plotting to the left of the Arai plot which are again non-unique to gCRMs (Riisager & Riisager, 2001; Yu & Tauxe, 2006). gCRMs have positive pTRM-tail checks, but these become negative and more TRM-like when the laboratory field direction is varied (Figure 8). A mixture of positive and negative pTRM-tail checks are, however, not unique to gCRMs (Riisager & Riisager, 2001; Yu & Tauxe, 2006). This combination of concave-up curvature, negative pTRM checks and non-zero pTRM tail checks lead to gCRM Arai plots failing current acceptance criteria for strongly interacting distributions, but these features are less pronounced for weakly interacting distributions and gCRMs can pass selection criteria leading to incorrect PI estimates (Figure 7 and Table 1).

This gCRM Araiplot curvature is due to lower coercivity particles carrying the majority of the gCRM, which is lost at low temperatures during simulated heating. In contrast, the majority of the new pTRM is recorded by higher coercivity particles and acquired at higher temperatures, that is, the gCRM is easily demagnetized at low temperatures, but the pTRM is not acquired until higher temperatures. Increasing magnetostatic interactions

10.1029/2022JB025858

increases this curvature by shifting the gCRM unblocking spectra to lower temperatures and the pTRM blocking spectra to higher temperatures (Figures 6 and 7).

Compared to the gCRM Arai plots, the pure TRM Arai plots have substantially lower concave-up curvature (Figure 7). At low temperatures, pTRM acquired is slightly less than TRM lost, which produces the concave-up curvature. Magnetostatic interactions are greater at lower temperatures. As a result, during intermediate heating steps, interacting particles unblock at lower temperatures than when they initially acquired their TRM and experience higher interactions during pTRM acquisition. This leads to reduced pTRMs.

The concave-up curvature in our gCRM Arai plots was also previously reported for models of gCRMs carried by non- and interacting systems (e.g., McClelland, 1996; Shcherbakov et al., 2017, 2021). The high-temperature linear segments of our gCRM and gCRM(T) Arai plots underestimating the paleointensity is consistent with results from Shcherbakov et al. (2017); Shcherbakov and Sycheva (2019). The increase in curvature with interactions was not predicted by Shcherbakov and Sycheva (2019); they did not find any significant variations due to increased interactions in their model.

This concave-up curvature is also observed in experimental gCRM Arai plots, although there are limited experimental studies of Thellier-type methods on gCRMs because synthetic samples are often unstable during heating (Pick & Tauxe, 1991). Studying hematite grown at 97°C, Stokking and Tauxe (1990) observed both near-linear ($\bar{k}' = -0.13$) and concave-up ($\bar{k}' = 1.04$) Arai plots for different samples of synthetic hematite. In the latter, the large curvature was attributed to alteration at temperatures >300°C. In agreement with other theoretical publications (e.g., McClelland, 1996; Shcherbakov et al., 2017, 2021), we suggest this behavior is intrinsic to gCRMs. Gendler et al. (2005) observed a high degree of concave-up curvature ($\bar{k}' = 1.37$) and pTRM checks which plot at lower values for maghemite gCRMs formed by alteration of ferrihydrite at 350°C. This is more curved than our model predicts for gCRMs in maghemite at 350°C, we found $\bar{k}' = 0.43$ for PN2 and 0.92 for PW2. Gendler et al. (2005) suggested this high degree of curvature may be due to alteration of maghemite to hematite during gCRM acquisition. Gendler et al. (2005) estimated that up to 20% of the maghemite may have altered to hematite.

Despite the concave-up curvature, all our modeled gCRM Arai plots have two near-linear segments from which paleointensity estimates could be made. These over- and under-estimate paleointensity at low and high temperatures. Current selection criteria, for example, modified-TTB successfully reject the low-temperature fits for all Preisach distributions, but high-temperature fits for weakly interacting distributions pass and underestimate the field by ∼66% (Figure 7 and Table 1). The most important criteria for isolating gCRMs are based on pTRM checks and pTRM-tail checks, but these do not reject all gCRM estimates. Evaluating the degree of curvature over the whole temperature range where the primary magnetization is isolated can be used to detect gCRMs in all Preisach distributions. This can be done by incorporating $\bar{k}' < 0.27$ into the selection criteria as none of the gCRM Arai plots in this study passed this test; $\bar{k}'$ is also used to detect MD grains (Paterson, 2011). However, the potential of the curvature parameter $\bar{k}'$ to be of practical use in real samples is limited, as NRMs are usually partially overprinted. To differentiate gCRMs from TRMs carried by MD grains, the Thellier protocol can be repeated for a lab-induced TRM and if the curvature is not reproducible, the original magnetization is likely a gCRM.

7.3. Angular Dependence of TRM and Arai Plots

Varying the field angle between the initial TRM acquisition and simulated laboratory pTRM introduces curvature into the TRM Arai plots, particularly for the strongly interacting case (Figures 8a–8c). Increasing the field angle to 90° produces concave-down curvature at low temperatures and concave-up curvature at high temperatures. Further increasing the field angle to 180° produces concave-down curvature over the whole temperature range. PTRM checks plot to the left of the Arai plot and pTRM-tail checks become negative. This leads to failure of the modified-TTB selection criteria, and no accepted estimates for interacting distributions when $\phi_f = 90°$ and 180°. The overestimation of the pTRM gained at lower temperatures for 90° and at all temperatures at 180° (F1 in Figure 8) is due to some particles only unblocking during in-field heating and becoming re-magnetized in a different direction. The concave-up curvature seen at higher temperatures in the 90° case, is due to the angular dependency of the thermal critical barriers. Particles with easy-axes close to 90° and 0° from the laboratory field direction, experience lower energy barriers and unblock at lower temperatures. The majority of these particles are not closely aligned with the laboratory field direction and this reduces the pTRM gained.

8. Conclusion

We modeled gCRM acquisition using a Preisach model for assemblages of interacting SD particles. We showed gCRM intensity is sensitive to magnetostatic interactions, coercivity distributions and acquisition conditions (Figures 4, 5 and 10). Increasing interactions decreases gCRM intensity, in agreement with the literature (Shcherbakov et al., 2017). gCRMs carried by lower coercivity distributions, acquired at higher temperatures or over longer time scales all have stronger intensities. These factors all increase the blocking volume of a particle during gCRM acquisition, which increases the probability of field alignment. By deriving and incorporating a growth-rate dependent effective time into the model, we found gCRMs display a stronger dependency on growth rate (Figure 4) (McClelland, 1996).

We show that gCRMs are approximately four times less sensitive to magnetostatic interactions than TRMs, because particles block at ∼4% of their terminal volume during gCRM acquisition (Figure 5). gCRMs have a lower thermal stability than TRMs (Figure 6) because the majority of a gCRM is carried by lower coercivity particles which unblock at lower temperatures. These differences in gCRM and TRM behavior produce concave-up gCRM Arai plots for all Preisach distributions (Figure 7), consistent with previous theoretical models (McClelland, 1996; Shcherbakov et al., 2017) and some experimental studies (Gendler et al., 2005; Stokking & Tauxe, 1990). This is the first study to incorporate pTRM checks and pTRM-tail checks into modeling paleointensity determination methods in gCRMs. We find gCRM Arai plots have pTRM checks which plot to the left of the Arai plot and positive pTRM-tail checks which become negative when the angle between the TRM acquisition field and laboratory field is increased (Figure 8). gCRM Arai plots have two near-linear segments with the potential to make PI estimations from. For strongly interacting distributions all fits fail current selection criteria, however, for weakly interacting distributions acceptable fits occur at high temperatures and underestimate the field by up to 66%. Including the degree of curvature over the whole temperature range where the primary magnetization is isolated and rejecting Arai plots where $\bar{k}' > 0.27$ detects gCRMs for all Preisach distributions and prevents incorrect PIs from gCRMs. Though the parameter $\bar{k}'$ has limitations when working with multi-component NRMs.

Data Availability Statement

The Preisach gCRM Python model developed and used here is available for download from Zenodo (https://doi.org/10.5281/zenodo.7428933), which links to Github where any updates will be placed (https://github.com/EvieBaker/Preisach_gCRM_model).

Acknowledgments

Evelyn B. Baker is sponsored by a Science and Technology Facilities Council PhD scholarship 2295497. Adrian R. Muxworthy acknowledges support from Natural Environmental Research Council grants NE/S001018/1 and NE/V001388/1.

References

Almeida, T. P., Kasama, T., Muxworthy, A. R., Williams, W., Nagy, L., Hansen, T. W., et al. (2014). Visualized effect of oxidation on magnetic recording fidelity in pseudo-single-domain magnetite particles. *Nature Communications*, *5*(1), 1–6. https://doi.org/10.1038/ncomms6154

Barbier, J. C. (1954). Le traînage magnétique de fluctuation. *Annales de Physique*, *12*(9), 84–140. https://doi.org/10.1051/anphys/195412090084

Baumgartner, J., Dey, A., Bomans, P. H., Le Coadou, C., Fratzl, P., Sommerdijk, N. A. J. M., & Faivre, D. (2013). Nucleation and growth of magnetite from solution. *Nature Materials*, *12*(4), 310–314. https://doi.org/10.1038/nmat3558

Berndt, T., & Muxworthy, A. R. (2017). Dating Icelandic glacial floods using a new viscous remanent magnetization protocol. *Geology*, *45*(4), 339–342. https://doi.org/10.1130/G38600.1

Bertotti, G. (1998). *Hysteresis in magnetism: For physicists, materials scientists, and engineers* (1st ed.). Academic Press.

Bleil, U., & Petersen, N. (1983). Variations in magnetization intensity and low-temperature titanomagnetite oxidation of ocean floor basalts. *Nature*, *301*(5899), 384–388. https://doi.org/10.1038/301384a0

Borcia, I., Spinu, L., & Stancu, A. (2002). A Preisach–Néel Model with Thermally Variable Variance. *IEEE Transactions on Magnetics*, *38*(5), 2415–2417. https://doi.org/10.1109/TMAG.2002.803611

Coe, R. S. (1967). The determination of paleointensities of the Earth's magnetic field with emphasis on mechanisms which could cause non-ideal behavior in Thellier's method. *Journal of Geomagnetism and Geoelectricity*, *19*(3), 157–179. https://doi.org/10.5636/jgg.19.157

Corless, R. M., Gonnet, G. H., Hare, D. E., Jeffrey, D. J., & Knuth, D. E. (1996). On the LambertW function. *Advances in Computational Mathematics*, *5*(1), 329–359. https://doi.org/10.1007/BF02124750

Di Chiara, A., Muxworthy, A. R., Trindade, R. I. F., & Bispo-Santos, F. (2017). *Geochemistry, Geophysics, Geosystems*, *18*(11), 3891–3903. https://doi.org/10.1002/2017GC007175

Dodson, M. H., & McClelland-Brown, E. (1980). Magnetic blocking temperatures of single-domain grains during slow cooling. *Journal of Geophysical Research*, *85*(B5), 2625–2637. https://doi.org/10.1029/JB085iB05p02625

Draeger, U., Prévot, M., Poidras, T., & Riisager, J. (2006). Single-domain chemical, thermochemical and thermal remanences in a basaltic rock. *Geophysical Journal International*, *166*(1), 12–32. https://doi.org/10.1111/j.1365-246X.2006.02862.x

Dunlop, D. J. (1969). Interactions in rocks and the reliability of paleointensity data. *Earth and Planetary Science Letter*s, 7(2), 178–182. https://doi.org/10.1016/0012-821X(69)90034-X

Dunlop, D. J., & Özdemir, Ö. (1997). *Rock magnetism: Fundamentals and frontiers* (Vol. 1). Cambridge University Press.

Eberl, D., Kile, D. E., & Drits, V. (2002). On geological interpretations of crystal size distributions: Constant vs. proportionate growth. *American Mineralogist*, *87*(8–9), 1235–1241. https://doi.org/10.2138/am-2002-8-923

Elmore, R. D., Muxworthy, A. R., & Aldana, M. (2012). Remagnetization and chemical alteration of sedimentary rocks. *Geological Society, London, Special Publications*, *371*(1), 1–21. https://doi.org/10.1144/SP371.15

Fabian, K. (2009). Thermochemical remanence acquisition in single-domain particle ensembles: A case for possible overestimation of the geomagnetic paleointensity. *Geochemistry, Geophysics, Geosystems*, *10*(6). https://doi.org/10.1029/2009GC002420

Ferk, A., Leonhardt, R., Hess, K.-U., Koch, S., Egli, R., Krása, D., & Dingwell, D. B. (2014). Influence of cooling rate on thermoremanence of magnetite grains: Identifying the role of different magnetic domain states. *Journal of Geophysical Research: Solid Earth*, *119*(3), 1599–1606. https://doi.org/10.1002/2013JB010845

Gaunt, P. (1986). Magnetic viscosity and thermal activation energy. *Journal of Applied Physics*, *59*(12), 4129–4132. https://doi.org/10.1063/1.336671

Ge, K., Williams, W., Liu, Q., & Yu, Y. (2014). Effects of the core-shell structure on the magnetic properties of partially oxidized magnetite grains: Experimental and micromagnetic investigations. *Geochemistry, Geophysics, Geosystems*, *15*(5), 2021–2038. https://doi.org/10.1002/2014GC005265

Gendler, T. S., Shcherbakov, V. P., Dekkers, M. J., Gapeev, A. K., Gribov, S. K., & McClelland, E. (2005). The lepidocrocite–maghemite–haematite reaction chain—I. Acquisition of chemical remanent magnetization by maghemite, its magnetic properties and thermal stability. *Geophysical Journal International*, *160*(3), 815–832. https://doi.org/10.1111/j.1365-246X.2005.02550.x

Gribov, S. K., Dolotov, A. V., & Shcherbakov, V. P. (2017). Experimental modeling of the chemical remanent magnetization and Thellier procedure on titanomagnetite-bearing basalts. *Izvestiya — Physics of the Solid Earth*, *53*(2), 274–292. https://doi.org/10.1134/S1069351317010062

Haigh, G. (1958). The process of magnetization by chemical change. *Philosophical Magazine*, *3*(27), 267–286. https://doi.org/10.1080/14786435808238219

Halgedahl, S. L., Day, R., & Fuller, M. (1980). The effect of cooling rate on the intensity of weak-field trm in single-domain magnetite. *Journal of Geophysical Research*, *85*(B7), 3690–3698. https://doi.org/10.1029/JB085iB07p03690

Heider, F., & Dunlop, D. J. (1987). Two types of chemical remanent magnetization during the oxidation of magnetite. *Physics of the Earth and Planetary Interiors*, *46*(1), 24–45. https://doi.org/10.1016/0031-9201(87)90169-5

Hoye, G., & Evans, M. (1975). Remanent magnetizations in oxidized olivine. *Geophysical Journal International*, *41*(1), 139–150. https://doi.org/10.1111/j.1365-246X.1975.tb05490.x

Jiang, Z., Liu, Q., Dekkers, M. J., Tauxe, L., Qin, H., Barrón, V., & Torrent, J. (2015). Acquisition of chemical remanent magnetization during experimental ferrihydrite–hematite conversion in Earth-like magnetic field—implications for paleomagnetic studies of red beds. *Earth and Planetary Science Letters*, *428*, 1–10. https://doi.org/10.1016/j.epsl.2015.07.024

Jönsson, P. E. (2003). Superparamagnetism and spin glass dynamics of interacting magnetic nanoparticle systems. In S. A. Rice (Ed.), *Advances in chemical physics* (pp. 191–248). John Wiley Sons, Ltd. https://doi.org/10.1002/0471484237.ch3

Kono, M. (1974). Intensities of the Earth's magnetic field about 60 m.y. ago determined from the Deccan Trap Basalts, India. *Journal of Geophysical Research*, *79*(8), 1135–1141. https://doi.org/10.1029/JB079i008p01135

Kosterov, A. A., & Prévot, M. (1998). Possible mechanisms causing failure of thellier palaeointensity experiments in some basalts. *Geophysical Journal International*, *134*(2), 554–572. https://doi.org/10.1046/j.1365-246x.1998.00581.x

Larson, E. E., Walker, T. R., Patterson, P. E., Hoblitt, R. P., & Rosenbaum, J. G. (1982). Paleomagnetism of the Moenkopi Formation, Colorado Plateau: Basis for long-term model of acquisition of chemical remanent magnetism in red beds. *Journal of Geophysical Research*, *87*(B2), 1081–1106. https://doi.org/10.1029/JB087iB02p01081

Levi, S. (1977). The effect of magnetite particle size on paleointensity determinations of the geomagnetic field. *Physics of the Earth and Planetary Interiors*, *13*(4), 245–259. https://doi.org/10.1016/0031-9201(77)90107-8

Lyberatos, A., Chantrell, R. W., & O' Grady, K. (1994). Activation volumes and magnetization reversal in fine particles. In G. C. Hadjipanayis & R. W. Siegel (Eds.), *Nanophase materials: Synthesis — properties — applications* (pp. 653–662). Springer Netherlands. https://doi.org/10.1007/978-94-011-1076-1_67

McClelland, E. (1996). Theory of CRM acquired by grain growth, and its implications for TRM discrimination and palaeointensity determination in igneous rocks. *Geophysical Journal International*, *126*(1), 271–280. https://doi.org/10.1111/j.1365-246X.1996.tb05285.x

Mcclelland, E., & Goss, C. (1993). Self Reversal of Chemical Remanent Magnetization on the Transformation of Maghemite to Haematite. *Geophysical Journal International*, *112*(3), 517–532. https://doi.org/10.1111/j.1365-246X.1993.tb01185.x

Muxworthy, A. R., Bland, P. A., Davison, T. M., Moore, J., Collins, G. S., & Ciesla, F. J. (2017). Evidence for an impact-induced magnetic fabric in allende, and exogenous alternatives to the core dynamo theory for allende magnetization. *Meteoritics & Planetary Science*, *52*(10), 2132–2146. https://doi.org/10.1111/maps.12918

Muxworthy, A. R., & Dunlop, D. J. (2002). First-order reversal curve (FORC) diagrams for pseudo-single-domain magnetites at high temperature. *Earth and Planetary Science Letters*, *203*(1), 369–382. https://doi.org/10.1016/S0012-821X(02)00880-4

Muxworthy, A. R., & Heslop, D. (2011). A Preisach method for estimating absolute paleofield intensity under the constraint of using only isothermal measurements: 1. Theoretical framework. *Journal of Geophysical Research*, *116*(B4). https://doi.org/10.1029/2010JB007843

Muxworthy, A. R., Heslop, D., & Michalk, D. M. (2009). Thermal fluctuation fields in basalts. *Earth Planets and Space*, *61*(1), 111–117. https://doi.org/10.1186/BF03352890

Muxworthy, A. R., Heslop, D., Paterson, G. A., & Michalk, D. (2011). A Preisach method for estimating absolute paleofield intensity under the constraint of using only isothermal measurements: 2. Experimental testing. *Journal of Geophysical Research*, *116*(B4). https://doi.org/10.1029/2010JB007844

Muxworthy, A. R., & Williams, W. (2005). Magnetostatic interaction fields in first-order-reversal-curve diagrams. *Journal of Applied Physics*, *97*(6), 063905. https://doi.org/10.1063/1.1861518

Nagy, L., Williams, W., Tauxe, L., & Muxworthy, A. (2022). Chasing tails: Insights from micromagnetic modeling for thermomagnetic recording in non-uniform magnetic structures. *Geophysical Research Letters*, *49*(23), e2022GL101032. https://doi.org/10.1029/2022GL101032

Néel, L. (1949). Théorie du traînage magnétique des ferromagnétiques en grains fins avec applications aux terres cuites. *Annals of Geophysics*, *5*, 99–136.

Néel, L. (1958). Sur les effets d'un couplage entre grains ferromagnétiques doués d'hystérésis. *Comptes Rendus Hebdomadaires Des Seances De L Academie Des Sciences*, *246*(16), 2313–2319.

Nguyen, T., & Pechersky, D. (1987). Experimental study of chemical and crystallization remanent magnetizations in magnetite. *Physics of the Earth and Planetary Interiors*, *46*(1), 46–63. https://doi.org/10.1016/0031-9201(87)90170-1

Özdemir, Ö., & Banerjee, S. K. (1984). High temperature stability of maghemite (γ-Fe_2O_3). *Geophysical Research Letters*, *11*(3), 161–164. https://doi.org/10.1029/GL011i003p00161

Özdemir, Ö., & Dunlop, D. J. (1993). Chemical remanent magnetization during γFeOOH phase transformations. *Journal of Geophysical Research*, *98*(B3), 4191–4198. https://doi.org/10.1029/92JB02569

10.1029/2022JB025858

Paterson, G. A. (2011). A simple test for the presence of multidomain behavior during paleointensity experiments. *Journal of Geophysical Research*, *116*(B10). https://doi.org/10.1029/2011JB008369

Paterson, G. A., Tauxe, L., Biggin, A. J., Shaar, R., & Jonestrask, L. C. (2014). On improving the selection of thellier-type paleointensity data. *Geochemistry, Geophysics, Geosystems*, *15*(4), 1180–1192. https://doi.org/10.1002/2013GC005135

Penny, C., Muxworthy, A. R., & Fabian, K. (2019). Mean-field modelling of magnetic nanoparticles: The effect of particle size and shape on the curie temperature. *Physical Review B: Condensed Matter*, *99*, 174414. https://doi.org/10.1103/PhysRevB.99.174414

Pfeiffer, H. (1990). Determination of anisotropy field distribution in particle assemblies taking into account thermal fluctuations. *Physica Status Solidi A*, *118*(1), 295–306. https://doi.org/10.1002/pssa.2211180133

Pick, T., & Tauxe, L. (1991). Chemical remanent magnetization in synthetic magnetite. *Journal of Geophysical Research*, *96*(B6), 9925–9936. https://doi.org/10.1029/91JB00706

Preisach, F. (1935). Über die magnetische Nachwirkung. *Zeitschrift für Physik*, *94*(5–6), 277–302. https://doi.org/10.1007/BF01349418

Pucher, R. (1969). Relative stability of chemical and thermal remanence in synthetic ferrites. *Earth and Planetary Science Letters*, *6*(2), 107–111. https://doi.org/10.1016/0012-821X(69)90127-7

Rickard, D. (2019). How long does it take a pyrite framboid to form? *Earth and Planetary Science Letters*, *513*, 64–68. https://doi.org/10.1016/j.epsl.2019.02.019

Riisager, P., & Riisager, J. (2001). Detecting multidomain magnetic grains in thellier palaeointensity experiments. *Physics of the Earth and Planetary Interiors*, *125*(1), 111–117. https://doi.org/10.1016/S0031-9201(01)00236-9

Roberts, A. P., Pike, C. R., & Verosub, K. L. (2000). First-order reversal curve diagrams: A new tool for characterizing the magnetic properties of natural samples. *Journal of Geophysical Research*, *105*(B12), 28461–28475. https://doi.org/10.1029/2000JB900326

Roshko, R. M., & Viddal, C. (2004). Interpreting remanence isotherms: A Preisach-based study. *European Physical Journal B: Condensed Matter and Complex Systems*, *40*(2), 145–151. https://doi.org/10.1140/epjb/e2004-00253-3

Shaar, R., & Tauxe, L. (2015). Instability of thermoremanence and the problem of estimating the ancient geomagnetic field strength from non-single-domain recorders. *Proceedings of the National Academy of Sciences*, *112*(36), 11187–11192. https://doi.org/10.1073/pnas.1507986112

Shcherbakov, V. P., Lhuillier, F., & Sycheva, N. K. (2021). Exact Analytical Solutions for Kinetic Equations Describing Thermochemical Remanence Acquisition for Single-Domain Grains: Implications for Absolute Paleointensity Determinations. *Journal of Geophysical Research: Solid Earth*, *126*(5), e2020JB021536. https://doi.org/10.1029/2020JB021536

Shcherbakov, V. P., & Sycheva, N. K. (2019). Study of Similarity between Blocking Temperature Spectra of Chemical and Thermoremanent Magnetizations by Computer Simulation. *Izvestiya — Physics of the Solid Earth*, *55*(5), 777–791. https://doi.org/10.1134/S1069351319050100

Shcherbakov, V. P., Sycheva, N. K., & Gribov, S. K. (2017). Experimental and numerical simulation of the acquisition of chemical remanent magnetization and the Thellier procedure. *Izvestiya — Physics of the Solid Earth*, *53*(5), 645–657. https://doi.org/10.1134/S1069351317040085

Shcherbakov, V. P., Sycheva, N. K., & Lamash, B. E. (1996). Monte Carlo modelling of TRM and CRM acquisition and comparison of their properties in an ensemble of interacting SD grains. *Geophysical Research Letters*, *23*(20), 2827–2830. https://doi.org/10.1029/96GL01999

Stancu, A., & Spinu, L. (1998). Temperature- and time-dependent preisach model for a stoner-wohlfarth particle system. *IEEE Transactions on Magnetics*, *34*(6), 3867–3875. https://doi.org/10.1109/20.728296

Stokking, L. B., & Tauxe, L. (1987). Acquisition of chemical remanent magnetization by synthetic iron oxide. *Nature*, *327*(6123), 610–612. https://doi.org/10.1038/327610a0

Stokking, L. B., & Tauxe, L. (1990). Properties of chemical remanence in synthetic hematite: Testing theoretical predictions. *Journal of Geophysical Research*, *95*(B8), 12639–12652. https://doi.org/10.1029/JB095iB08p12639

Stoner, E. C., & Wohlfarth, E. P. (1948). A mechanism of magnetic hysteresis in heterogeneous alloys. *Philosophical Transactions of the Royal Society of London — Series A: Mathematical and Physical Sciences*, *240*(826), 599–642. https://doi.org/10.1109/TMAG.1991.1183750

Tanaka, H., & Yamamoto, Y. (2016). Palaeointensities from pliocene lava sequences in Iceland: Emphasis on the problem of arai plot with two linear segments. *Geophysical Journal International*, *205*(2), 694–714. https://doi.org/10.1093/gji/ggw031

Thellier, E., & Thellier, O. (1959). Sur l'intensite du champ magnetique terrestre dans le passe historique et geologique. *Annales Geophysicae*, *15*, 285–376.

Weisstein, E. W. (2009). "Gaussian function," MathWorld-A wolfram web resource. Retrieved from http://mathworld.wolfram.com/GaussianFunction.html

Wohlfarth, E. P. (1979). The temperature dependence of the magnetic susceptibility of spin glasses. *Physics Letters A*, *70*(5), 489–491. https://doi.org/10.1016/0375-9601(79)90375-X

Wohlfarth, E. P. (1984). The coefficient of magnetic viscosity. *Journal of Physics F: Metal Physics*, *14*(8), L155. https://doi.org/10.1088/0305-4608/14/8/005

Xu, S., & Dunlop, D. J. (2004). Thellier paleointensity theory and experiments for multidomain grains. *Journal of Geophysical Research*, *109*(B7). https://doi.org/10.1029/2004JB003024

Yamamoto, Y. (2006). Possible TCRM acquisition of the kilauea 1960 lava, Hawaii: Failure of the thellier paleointensity determination inferred from equilibrium temperature of the Fe-Ti oxide. *Earth Planets and Space*, *58*(8), 1033–1044. https://doi.org/10.1186/BF03352608

Yu, Y., & Tauxe, L. (2006). Effect of multi-cycle heat treatment and pre-history dependence on partial thermoremanence (pTRM) and pTRM tails. *Physics of the Earth and Planetary Interiors*, *157*(3), 196–207. https://doi.org/10.1016/j.pepi.2006.04.006

Yu, Y., Tauxe, L., & Genevey, A. (2004). Toward an optimal geomagnetic field intensity determination technique. *Geochemistry, Geophysics, Geosystems*, *5*(2). https://doi.org/10.1029/2003GC000630